bioRxiv preprint doi: https://doi.org/10.1101/2020.07.10.197616; this version posted July 14, 2020. The copyright holder for this preprint (which was not certified by peer review) is the author/funder, who has granted bioRxiv a license to display the preprint in perpetuity. It is made available under aCC-BY 4.0 International license.

Calponin-Homology Domain mediated bending of membrane associated actin filaments

Saravanan Palani, Mohan K. Balasubramanian*, and Darius V. Köster*

Centre for Mechanochemical Cell Biology and Warwick Medical School, Division of Biomedical Sciences, CV4 7AL Coventry, UK
* Corresponding authors: M.K.Balasubramanian@warwick.ac.uk, D.Koester@warwick.ac.uk

Actin filaments are central to numerous biological processes in all domains of life. Driven by the interplay with molecular motors, actin binding and actin modulating proteins, the actin cytoskeleton exhibits a variety of geometries. This includes structures with a curved geometry such as axon-stabilizing actin rings, actin cages around mitochondria and the cytokinetic actomyosin ring, which are generally assumed to be formed by short linear filaments held together by actin cross-linkers. However, whether individual actin filaments in these structures could be curved and how they may assume a curved geometry remains unknown. Here, we show that "curly", a region from the IQGAP family of proteins from three different organisms, comprising the actin-binding calponin-homology domain and a C-terminal unstructured domain, stabilizes individual actin filaments in a curved geometry when anchored to lipid membranes. Whereas F-actin is semi-flexible with a persistence length of ~10 μm, binding of mobile curly within lipid membranes generates actin filament arcs and full rings of high curvature with radii below 1 μm. Higher rates of fully formed actin rings are observed in the presence of the actin-binding coiled-coil protein tropomyosin, and also when actin is directly polymerized on lipid membranes decorated with curly. Strikingly, curly induced actin filament rings contract upon the addition of muscle myosin II filaments and expression of curly in mammalian cells leads to highly curved actin structures in the cytoskeleton. Taken together, our work identifies a new mechanism to generate highly curved actin filaments, which opens a new range of possibilities to control actin filament geometries, that can be used, for example, in designing synthetic cytoskeletal structures.

The IQGAP family of proteins plays a key role in actin cytoskeleton regulation including the assembly and function of the contractile actomyosin ring in budding and fission yeasts (Briggs & Sacks, 2003; Eng et al., 1998; Epp & Chant, 1997; Tebbs et al., 2013). To study the mechanism and role of actin binding by the fission yeast IQGAP (encoded by the *rng2* gene), we utilized a strategy to investigate its function when immobilized on supported lipid bilayers. We chose this approach, since during cytokinesis Rng2, which binds a number of actomyosin ring proteins, is tethered to the plasma membrane via Mid1 ensuring the formation and anchoring of the cytokinetic ring (Laplante et al., 2016; Laporte et al., 2011; Padmanabhan et al., 2011). We linked hexa-histidine tagged *rng2* protein fragments to supported lipid bilayers containing nickel-chelating lipids (DOGS-NTA(Ni^{2+})) and observed the binding of fluorescently labelled actin filaments using live total internal reflection fluorescence (TIRF) microscopy as described earlier (Köster et al., 2016) (Figure 1A). The actin-binding calponin homology domain (CHD) is located at the N-terminus of Rng2 (AA 41-147), and the construct His_6-Rng2[1-189] (subsequently referred to as curly) containing the CHD and additional 42 amino acids was found to bind actin filaments (Figure 1B, Figure 1-figure supplement 1A-C). Remarkably, when bound to His_6-Curly a large fraction of actin filaments formed tightly bent rings (21 ± 5 rings per field of view) with a characteristic curvature C_{curly} = 1.7 ± 0.5 μm^{-1} (N = 425) (Figure 1 C; Figure 1 – figure supplement 1 D; Video 1). To our knowledge, this is an unprecedented phenomenon specific to curly. Binding of other membrane attached actin binding proteins in the same geometry does not appreciably bend actin ($C_{\alpha\text{-actinin}}$ = 0.3 ± 0.1 μm^{-1}, N = 85; $C_{EzrinABD}$ = 0.5 ± 0.3 μm^{-1}, N = 127) (Figure 1-figure supplement 2 A-D). Membrane anchored fimbrin has also been shown not to bend actin (Murrell & Gardel, 2012).

bioRxiv preprint doi: https://doi.org/10.1101/2020.07.10.197616; this version posted July 14, 2020. The copyright holder for this preprint (which was not certified by peer review) is the author/funder, who has granted bioRxiv a license to display the preprint in perpetuity. It is made available under aCC-BY 4.0 International license.

To understand the mechanism leading to actin filament bending and ring formation by curly, we tested the role of different fragments of curly and their orientation as well as curly anchoring to lipid membranes in actin filament bending. Curly mobility within planar lipid membranes was important for actin bending as glass adsorbed, immobilized His_6-Curly displayed reduced actin bending and ring formation (C_{glass} = 0.6 ± 0.3 μm^{-1}, N = 138) (Figure 2 A, F), and when using membrane tethered fluorescently labelled His_6-SNAP-curly, a weak accumulation of curly under actin filaments could be observed (Figure 2- figure supplement 1). Next, we generated fragments of curly to discern the regions important for actin binding and bending. We found that the C-terminal region following the CHD (His6-Rng2[150-250]) alone was able to bind actin filaments without inducing bending ($C_{[150-250]}$ = 0.2 ± 0.1 μm^{-1}, N = 17) (Figure 2 B). Interestingly, a 7AA deletion (Rng2[1-189]-Δ(154-160)) led to a reduced degree of actin binding and bending ($C_{\Delta(154-160)}$ = 0.4 ± 0.1 μm^{-1}, N = 33) (Figure 2 C). Similarly, the fragments Rng2[41-189] and Rng2[1-147] displayed weaker actin binding and bending compared to curly ($C_{[41-189]}$ = 0.6 ± 0.2 μm^{-1}, N = 323; $C_{[1-147]}$ = 0.7 ± 0.2 μm^{-1}, N = 118) (Figure 2 D, E). The location of the hexa-histidine tag to link curly to the lipid membrane (C-terminal hexa-histidine tagged construct Rng2[1-189]-His_6) did not affect actin filament bending (25 ± 7 rings per field of view; $C_{curly-his}$ = 1.5 ± 0.5 μm^{-1}, N = 184) (Figure 2 F). Taken together (Figure 2 G), this suggests that curly contains two actin binding sites, one located within the CHD followed by a second within Rng2[148-189]. Both actin binding sites are necessary for actin bending as neither Rng2[1-147] nor Rng2[150-250] caused strong bending. It is very likely that the second actin binding site includes the 7AA Rng2[154-160] as this unstructured region maps directly to AA 240-246 of the dystrophin CH2 domain (Wang et al., 2004). The first 40 AA of Rng2 are likely to be important for the protein folding and stability, because of which the Rng2[41-189] construct showed poor actin binding and did not lead to actin bending.

Careful examination of individual actin filaments bound to membrane tethered His_6-Curly allowed us to identify the occurrence of discrete kinks of an angle α = 37˚ ± 8˚ (N = 63) along actin filaments during the transition from straight to bent filaments (Figure 2-figure supplement 2 A, B; Video 2). Based on the experimental data and the predicted molecular structure of curly (Rng2[1-189]) we hypothesize that i) the CHD (Rng2[41-147]) contains at least one actin binding site (similar to the utrophin actin binding domains ABD2' (UTRN[84-94]) and ABD2 (UTRN[107-126]) (Kumari et al., 2020)) and ii) the C-terminal extension from the CHD contains an additional actin binding site (including Rng2[154-160]) (Wang et al., 2004). The latter could lead to a change in the actin subunit orientation within the actin filament similar to the action of cofilin (Narita, 2020) and could lead to overall actin bending when the binding is asymmetric (Figure 2-figure supplement 2 C). However, in contrast to cofilin, we could not observe any events actin filament severing by curly.

Next, we studied whether actin bending by curly depended on the orientation of actin filaments by following the landing of actin filaments decorated with labelled capping protein as a plus end marker (Bieling et al., 2016). We found that the bending was oriented anti-clockwise with respect to the plus end in all instances where the plus end was clearly labelled and the orientation of filament bending could be identified (Figure 3A, B; Figure 3-figure supplement 1 A, B). This was observed using both, the N-terminal and C-terminal hexa-histidine tagged curly indicating that the internal sequence of the two actin binding sites within curly sets the chirality of actin bending and not the position of the membrane linker (Figure 3A, B; Figure 3-figure supplement 1 A, B; Video 3, 4). Actin filaments appeared to bend concomitant with their landing on the supported lipid bilayer, which indicates that the bending did not require the full actin filament to be tethered to the SLB and underlined the earlier observation that the bending occurred locally.

To decouple the actin filament bending from the landing of actin filaments, we induced polymerization of actin filaments at planar lipid membranes in the presence of membrane tethered curly (His_6-Curly) by using membrane tethered formin (His_6-SpCdc12(FH1-FH2)), profilin-actin and ATP. Strikingly, polymerizing actin filaments displayed characteristic bending shortly after the onset of polymerization and grew often into full rings (44 ± 6 rings per field of view, $C_{formin\ rings}$ = 1.7 ± 0.4 μm^{-1}, N = 477; $C_{formin\ short}$ = 1.1 ± 0.3 μm^{-1}, N = 125)

bioRxiv preprint doi: https://doi.org/10.1101/2020.07.10.197616; this version posted July 14, 2020. The copyright holder for this preprint (which was not certified by peer review) is the author/funder, who has granted bioRxiv a license to display the preprint in perpetuity. It is made available under aCC-BY 4.0 International license.

(Figure 3 C, D; Figure 3-figure supplement 1 C, D; Video 5). By contrast, polymerization of actin filaments along SLBs decorated with His_{10}-SNAP-EzrinABD did not result in the formation of arcs and rings, establishing that actin filament bending was due to curly and not due to formin (Figure 3-figure supplement 1 E, F). These observations showed that actin bending occurs continuously due to the binding of membrane tethered curly and did not require the cross-linking of adjacent ends of the same filament as was observed with the actin cross-linker anillin (Kučera et al., 2020). Importantly, the uni-directional bending supports the hypothesis that the binding site of curly with actin filaments defines an orientation, and the propagation of a curved trajectory once established indicates a cooperative process.

Actin filaments forming the cytokinetic ring in *S. pombe* are wrapped by the coiled-coil protein tropomyosin (Cdc8), while the actin cross-linker fimbrin is present outside the cytokinetic ring region in Arp2/3 generated actin patches and prevents tropomyosin of binding to actin filaments in these patches (Skau & Kovar, 2010). To find out whether the actin bending effect of curly is conserved in tropomyosin wrapped actin filaments, we incubated actin filaments with tropomyosin before adding them to His_6-Curly containing SLBs. Strikingly, addition of tropomyosin to actin filaments increased the frequency of actin ring formation without affecting actin filament curvature (38 ± 3 rings per field of view; $C_{tropomyosin}$ = 1.4 ± 0.6 μm^{-1}, N = 204), while actin filaments incubated with the actin cross-linker fimbrin displayed reduced bending and ring formation (3 ± 2 rings per field of view; $C_{fimbrin}$ = 0.6 ± 0.4 μm^{-1}, N = 407) (Figure 3-figure supplement 2 A-E; Video 6). Thus, the tropomyosin Cdc8 and curly cooperate to enhance actin filament bending and ring formation.

Interestingly, we could observe that long actin filaments coated with tropomyosin would trace consecutive rings around the same center while landing on curly decorated lipid membranes. Subtraction of the image after completion of the first round of actin filament landing into a ring from the image after the second round revealed that the second ring occupied the interior space of the first ring. In line with that, comparison of the intensity profiles perpendicular to the actin filament of the first and second round of ring formation revealed a widening of the profile towards the interior of the ring (Figure 3-figure supplement 3 A, B). A similar effect could be observed in examples of actin filaments polymerized by membrane tethered formin in the presence of membrane tethered curly (Figure 3-figure supplement 3 C, D). This would suggest that curly can arrange long actin filaments into an inward oriented spiral.

To test whether the curly-induced actin rings can contract, we added rabbit skeletal muscle myosin II filaments and ATP to curly bound actin filaments and followed actin filament dynamics over time. After the myosin II filaments landed on the actin filaments, straight actin filaments were propelled by myosin action and eventually started to bend and displayed a variety of dynamics including translation, rotation and finally contraction of actin rings (Figure 3 E, Figure 3-figure supplement 4 A, Video 7). Interestingly, most actin rings displayed a counter-clockwise rotation (34/36 cases) and the contraction was slow with $v_{contraction}$ = 3 ± 0.7 nm s^{-1} (N = 29) (Figure 3 F; Video 8). Despite reaching high curvatures of C_{myoII} = 2.8 ± 0.7 μm^{-1} (N = 342) with a maximum of 6.3 μm^{-1} there was no evidence of breaking of actin filaments during the contraction process (Figure 3 G). Additionally, the myosin II induced flows of actin filaments increased the formation of actin rings significantly (79 ± 8 rings per field of view) indicating that myosin II filament induced actin filament sliding enhanced the ability of membrane anchored curly to generate actin filament bending (Figure 3-figure supplement 4 B, C). In line with this, actin filament rings displayed increased localization of fluorescently labelled curly after addition of myosin II filaments action indicating that curly showed an increased affinity for highly bent actin and/ or stabilized actin filaments at higher curvatures (Figure 3-figure supplement 4 D). Interestingly, despite the observed high curvatures of actin filaments upon myosin II filament action, severing of actin filament was not observed suggesting that binding of curly reduces the rigidity of actin filaments.

It was not obvious that addition of myosin II filaments would lead to actin ring constriction without the addition of any cross-linkers or other factors. When taking into account that curly

bioRxiv preprint doi: https://doi.org/10.1101/2020.07.10.197616; this version posted July 14, 2020. The copyright holder for this preprint (which was not certified by peer review) is the author/funder, who has granted bioRxiv a license to display the preprint in perpetuity. It is made available under aCC-BY 4.0 International license.

arranges actin filaments into an inward spiral, a possible explanation for actin ring constriction would be that the myosin II filament acts both as a cross-linker and motor protein: one end of the myosin II filament sits at the actin filament plus end while other myosin head domains of the same myosin II filament pull along the same actin filament to travel towards the plus end leading to constriction (Figure 3-figure supplement 4 E). This would result in sub-optimal myosin head orientations towards the actin filament, which could explain the observed slow constriction rates that were orders of magnitude slower than the reported values for actin propulsion by myosin II in motility assays (Toyoshima et al., 1990).

Since Rng2 belongs to the IQGAP protein family, we tested the N-terminal hexa-histidine tagged fragments of the IQGAP proteins Iqg1[1-330] (*S. cerevisiae*) and IQGAP1[1-678] (*H. sapiens*) and found that the bending of actin filaments was conserved ($C_{S.C.}$ = 1.1 ± 0.4 μm^{-1}; N = 110; $C_{H.S.}$ = 1.0 ± 0.2 μm^{-1}; N = 290) (Figure 4 A-C). Comparison of the available crystal structures of *H. sapiens* IQGAP1[28-190] with *S. pombe* Rng2[32-190] indicates a high similarity between the two (Figure 4-figure supplement 1).

Finally, to test the effect of curly on the actin cortex in cells, we expressed curly-EGFP in the mammalian cell lines HEK293T and RPE-1, which resulted in obvious changes in the actin cortex architecture with prominent occurrence of curved actin filaments and bundles with curvatures of $C_{HEK293T}$ = 2.3 ± 0.4 μm^{-1} (N = 91 from 14 cells), and C_{RPE-1} = 1.9 ± 0.6 μm^{-1} (N = 113 from 11 cells) (Figure 4D-F). Co-expression with LifeAct-mCherry confirmed that EGFP-Curly bound to actin filaments in cells (Figure 4-figure supplement 2). These experiments established that curly could instructively reorganize actin filaments / networks into curved structures and rings.

Discussion

Our results show that the N-terminal CHD of IQGAP proteins induces actin filament bending when tethered to lipid membranes, which constitutes a new type of actin binding protein and could be an important link between actin and membrane geometries. Recently, Uyeda and colleagues reported that curly (Rng2[1-189]) in solution can induce kinks at random locations of the actin filament (Hayakawa et al., 2020). This together with our results indicates that curly that is constrained to a lipid membrane, would bind asymmetrically to actin filaments leading to a succession of kinks towards the same direction leading to curling of the actin filaments into rings in the plane of the lipid membrane. With an estimated His_6-Curly surface density on SLBs of 5000 μm^{-2} (Köster et al., 2016; Nye & Groves, 2008) the approximated curly to actin ratio would be 1:7 or higher. The mobility of curly on the SLB allowing accumulation under actin filaments was important for continuous actin filament bending into rings as glass-immobilized curly failed to generate rings. In line with this, curly in solution, i.e. in the absence of a substrate providing confinement, did not lead to persistent bending of actin filaments (Hayakawa et al., 2020). Interestingly, individual transient kinks of an average angle of 37˚ ± 8˚ could be observed during actin filament binding to curly, but it remained unclear whether this is caused by binding of single or multiple proteins. Based on the data of the Utrophin-CHD actin binding sites (Kumari et al., 2020) together with the newly identified actin binding region withing Rng2[150-189], the local change of the actin filament structure induced by curly could be similar to the effect of cofilin (Narita, 2020) allowing the formation of actin rings with curvatures that would be energetically unfavorable given the actin filament persistence length of 10 µm (De La Cruz & Gardel, 2015). The increased flexibility of actin filaments is highlighted by the fact that addition of rabbit muscle myosin II filaments resulted in actin ring constriction without any evidence for filament rupture up to curvatures of 6.3 μm^{-1} which is much higher than expected for actin alone (Taylor et al., 2000). This mechanism of actin ring formation stands out as it bends individual actin filaments in contrast to other reported systems that generate actin rings made of bundles of actin filaments (Litschel et al., 2020; Mavrakis et al., 2014; Mishra et al., 2013; Way et al., 1995).

bioRxiv preprint doi: https://doi.org/10.1101/2020.07.10.197616; this version posted July 14, 2020. The copyright holder for this preprint (which was not certified by peer review) is the author/funder, who has granted bioRxiv a license to display the preprint in perpetuity. It is made available under aCC-BY 4.0 International license.

In case of *S. pombe* cytokinetic ring formation, Rng2 is localized at the plasma membrane by interaction with Mid1 via its C-terminal RAS-GAP and GRD domains (Almonacid et al., 2011; Padmanabhan et al., 2011) leaving the N-terminal CHD facing the cytoplasm and allowing interaction with actin filaments. Formin based polymerization of actin filaments is essential for cytokinetic ring formation and binding of the tropomyosin Cdc8 supports myosin driven cytokinetic ring contraction. Our work recapitulates that this minimal set of proteins can indeed generate and stabilize actin filaments of the right curvature to form the cytokinetic ring along the short axis of *S. pombe*. Even though electron microscopy data of the cytokinetic ring does not provide clear evidence of bent actin filaments (Swulius et al., 2018), this mechanism could work together with other processes such as cross-linkers ensuring the binding of fresh actin filaments along existing ones (Li & Munro, 2020) to drive robust formation of cytokinetic rings.

Highly bent actin filament structures are most likely important for many cellular structures such as axons (Vassilopoulos et al., 2019; Xu et al., 2013) and mitochondrial actin cages (Kruppa et al., 2018), but the molecular mechanisms leading to their formation are still poorly understood. Future work could provide insights whether curly plays a role in actin ring formation in axons and around mitochondria. In addition, our system of membrane bound curly, actin filaments, and myosin II filaments constitutes a minimalistic system for actin ring formation and constriction and could be used in future to design synthetic dividing vesicles and further exiting active membrane-cortex systems.

Materials and Methods:

Cloning and Protein purification

S. pombe Rng2 fragments, Fim1, Cdc12 (FH1-FH2) and S. cerevisiae Iqg1 were amplified from cDNA library and genomic DNA respectively. Amplified fragments were cloned into pET (6His) and pGEX (GST) based vectors using Gibson cloning method (NEB builder, E5520S). Plasmids used in this study is listed in Table S1.

All protein expression plasmids were transformed into E.coli BL21-(DE3). Single colony was inoculated in 20 ml of LB media supplemented with appropriate antibiotic (pET-Kanamycin; pGEX-Ampicillin). Precultures were grown for ~12-16 h at 36 °C shaking at 200 r.p.m. Cells were diluted to OD600 of 0.1 a.u. in 500 ml of LB with antibiotics and protein expression was induced with 0.25 mM isopropyl β-D-1-thiogalactopyranoside (IPTG). Protein was expressed for 3-4 h at 30 °C shaking at 200 r.p.m. unless otherwise noted. After induction cell pellets were collected and spun down at 7,000 r.p.m for 20 minutes after induction at 4 °C. Media was aspirated and pellets were washed once with cold phosphate buffered saline (PBS) with 1mM phenylmethylsulfonyl fluoride (PMSF), and pellets were stored at −80 °C.

His tagged protein (His6-Rng2, Igg1 and Iqgap1) purification: Cell pellets for purification were thawed on ice for 10 minutes. The pellets were resuspended in 10 ml of lysis buffer for sonication (50 mM Napi pH 7.6, 200 mM NaCl, 10mM Imidazole pH 7.5, 0.5 mM EDTA, 1 mM DTT, 1 mg/ ml lysozyme, and complete mini-EDTA-Free protease inhibitor cocktail tablets) and incubated on ice for 20 min, followed by sonication (8 cycles, 15 sec pulse). The lysates were centrifuged at 14000 r.p.m, 30 min, 4 °C and the clarified lysate was transferred to a 15-ml tube. The 400 µl slurry of HisPur™ Ni-NTA agarose resin (cat. no. 88221, Thermo fisher) was washed with wash buffer (5x) (50 mM Napi (pH 7.6), 300 mM NaCl, 30mM Imidazole pH 7, 0.5 mM EDTA and 1 mM DTT) before the lysate was added. The clarified lysate was added to the washed Ni-NTA resin and incubated for 2h at 4 °C. After incubation with NiNTA resin, beads were washed with wash buffer 6-8 times in BIO-RAD prepacked column. Protein was eluted using Ni-NTA elution buffer (50 mM NaPi pH 7.6, 300 mM NaCl, 0.5 mM EDTA, 1 mM DTT and 500 mM imidazole) and 300 µl elutions were collected in a clean Eppendorf tubes. Each fraction was assessed by SDS–polyacrylamide gel electrophoresis (SDS–PAGE). The eluates (E1-E3) were pooled, concentrated and buffer exchanged into the protein storage buffer (50 mM Tris-HCl pH 7.4, 150 mM NaCl, 1 mM DTT

bioRxiv preprint doi: https://doi.org/10.1101/2020.07.10.197616; this version posted July 14, 2020. The copyright holder for this preprint (which was not certified by peer review) is the author/funder, who has granted bioRxiv a license to display the preprint in perpetuity. It is made available under aCC-BY 4.0 International license.

and 10% glycerol) using a PD MiniTrap G-25 sephadex columns (GE Healthcare) and the protein was stored at −80 °C. The protein concentration was estimated by UV280 and by comparing known quantities of BSA standards on an SDS–PAGE gel.

GST tagged protein (GST-Fim1) purification: Cell pellets for purification were thawed on ice for 10 minutes. The pellets were resuspended in 10 ml of lysis buffer for sonication (PBS, 0.5 mM EDTA, 1 mM DTT, 1 mg/ ml lysozyme, and complete mini-EDTA-Free protease inhibitor cocktail tablets) and incubated on ice for 20 min, followed by sonication (10 cycles, 15 sec pulse). After sonication cell lysate was incubated with 0.5% Triton-X-100 for 20 minutes on ice. The lysates were centrifuged at 22000xg, 30 min, 4 °C and the clarified lysate was transferred to a 15-ml tube. The 400 µl slurry of glutathione sepharose-4B resin (cat. no. GE17-0756-01, GE) was washed with wash buffer (5x) (PBS, 0.5 mM EDTA and 1 mM DTT) before the lysate was added. The clarified lysate was added to the washed glutathione sepharose resin and incubated for 2-3h at 4 °C. After incubation with sepharose resin, beads were washed with wash buffer 6-8 times in poly-prep chromatography columns (BIO-RAD laboratories Inc). Protein was eluted using GST elution buffer (50 mM Tris-HCl pH8.0 and 10 mM glutathione). Purified protein sample was quantified and stored in the storage buffer as described above in the previous section.

Acetylation mimicking version of tropomyosin (ASCdc8) was expressed in BL21-DE3 and protein was purified by boiling and precipitation method as described earlier (Palani et al., 2019; Skoumpla et al., 2007). Purified tropomyosin was dialyzed against the storage buffer (50 mM NaCl, 10 mM imidazole, pH 7.5, and 1 mM DTT), flash frozen in liquid N2 and stored at -80 °C.

SNAP labelling (SNAP-Surface® 549, S9112S, NEB) of capping protein-beta and Rng2 1-189 was performed as per the manufactures protocol.

Co-sedimentation assay and Immunoblot

Co-sedimentation assays were performed at 25°C by mixing 3 µM actin with different Rng2 fragments, Sclqg1(1-330) and Hs IGAP1 (1-678), and then spun at 100,000 g (high speed) for 20 min at 25°C. Equal volumes of supernatant and pellet were separated by 12% SDS-PAGE gel and stained with Coomassie blue (SimplyBlueStain, Invitrogen) or immunoblotted. For western analysis, equal volumes of each sample were diluted in 1 × Laemmli buffer (Bio-Rad). Samples were run on a hand cast 10-well 12% acrylamide gels (Bio-Rad), transferred onto nitro cellulose membranes and blotted with 1:1000 Anti-His-HRP (6xHis Epitope TAG, Cat. no. sc-8036 HRP, Santa Cruz Inc) and 1:500 anti-actin-HRP (cat. no. sc-47778 HRP, Santa Cruz Inc). Signal was detected by enhanced chemiluminescence (Clarity western ECL, Bio-Rad) imaged on a ChemiDoc MP (Bio-Rad).

Mammalian expression

S. pombe Rng2 fragment (1-189) was cloned into pCDNA3.1-eGFP using gibson cloning method. HEK293 and RPE1 cells were transiently transfected with pCDNA3 containing SpRng2 (1-189) using Lipofectamine 2000 (cat. no. 11668019, Life Technologies) following manufacturer's instructions. Cells were transfected at ~70% confluency for 24 h before the experiments. For each imaging condition, 500,000 cells were transfected with 1 µg of DNA. Cells were seeded and imaged on µ-Dish 35 mm (cat. no. 81156, IBIDI). Before imaging, the culture medium was replaced with phenol red–free DMEM (Opti-MEM, cat. no. 31985062, Life Technologies). Images were taken using spinning disk microscope with a 100× Apo objective, NA 1.4.

In vitro assay and Total Internal Reflection Fluorescence (TIRF) microscopy

Supported Lipid Bilayer and Experimental Chamber Preparation

The sample preparation, experimental conditions and lipid composition were similar to the ones described in previous work [Koester et al, 2016]. Glass coverslips (#1.5 borosilicate,

bioRxiv preprint doi: https://doi.org/10.1101/2020.07.10.197616; this version posted July 14, 2020. The copyright holder for this preprint (which was not certified by peer review) is the author/funder, who has granted bioRxiv a license to display the preprint in perpetuity. It is made available under aCC-BY 4.0 International license.

Menzel, cat. no. 11348503, Fisher Scientific) for SLB formation were cleaned with Hellmanex III (Hellma Analytics, cat. No. Z805939, Merck) following the manufacturer's instructions followed by thorough rinses with EtOH and MilliQ water and blow dried with N2 gas. For the experimental chamber, 0.2 ml PCR tubes (cat. no. I1402-8100, Starlab) were cut to remove the lid and conical bottom part. The remaining ring was stuck to the cleaned glass using UV glue (cat. no. NOA88, Norland Products) and three minutes curing by intense UV light at 265 nm (UV Stratalinker 2400, Stratagene). Freshly cleaned and assembled chambers were directly used for experiments.
Supported lipid bilayers (SLB) containing 98% DOPC (cat. no. 850375, Avanti Polar Lipids) and 2% DGS-NTA(Ni2+) (cat. no. 790404, Avanti Polar Lipids) lipids were formed by fusion of small uni-lamellar vesicles (SUV) that were prepared by lipid extrusion using a membrane with 100 nm pore size (cat. no. 610000, Avanti Polar Lipids). SLBs were formed by addition of 10 µl of SUV mix (at 4 mM lipid concentration) to chambers filled with 90 µl KMEH (50 mM KCl, 2 mM $MgCl_2$, 1 mM EGTA, 20 mM HEPES, pH 7.2) and incubation for 30 min. Prior to addition of other proteins, the SLBs were washed 10 times by buffer exchange (always leaving 20 µl on top of the SLB to avoid damage by drying). We tested the formation of lipid bilayers and the mobility of lipids in control samples by following the recovery of fluorescence signal after photobleaching of hexa-histidine tagged GFP (His_6-GFP) as described in (Köster et al., 2016).

Actin filament polymerization and tethering to SLBs
Actin was purified from muscle acetone powder form rabbit (cat. no. M6890, Merck) and labelled with Alexa488-maleimide (cat. no. A10254, Thermo Fisher) following standard protocols (Köster et al., 2016; Pardee & Spudich, 1982).
In a typical experiment, actin filaments were polymerized in parallel to SLB formation to ensure that all components of the experiment were freshly assembled before starting imaging. First $10\%_{vol}$ of 10x ME buffer (100 mM $MgCl_2$, 20 mM EGTA, pH 7.2) were mixed with unlabeled and labeled G-actin (to a final label ratio of 20%), optionally supplemented with labelled capping protein in G-actin buffer (1 mM $CaCl_2$, 0.2mM ATP, 2mM Tris, 0.5 mM TCEP-HCl, pH 7.2) to a final G-actin concentration of 10 µM and incubated for 2 min to replace G-actin bound Ca^{2+} ions with Mg^{2+} ions. Polymerization of actin filaments was induced by addition of an equal amount of 2x KMEH buffer supplemented with 2 mM Mg-ATP bringing the G-actin concentration to 5 µM. After 30 min incubation time, actin filaments were added to the SLBs using blunt-cut pipette tips at a corresponding G-actin concentration of 100 nM (to ensure a homogenous mix of actin filaments, 2 µl of actin filament solution was mixed in 18 µl KMEH and then added to the SLB containing 80 µl KMEH). After 10 min of incubation, His_6-Curly or other variants of histidine-tagged actin binding proteins at a final concentration of 10 nM were added and a short time after (1 - 5 min) binding of actin to the SLB could be observed using TIRF microscopy.

In experiments with formin, the SLB was first incubated with 10 nM His_6-SpCdc12(FH1-FH2) and 10 nM His_6-Curly for 20 min, then washed twice with KMEH. During the incubation time, $10\%_{vol}$ of 10x ME buffer was mixed with unlabeled and labeled G-actin at 4 µM (final label ratio of 20%) together with 5 µM profilin and incubated for 5 min prior to addition to the SLB and imaging with TIRF microscopy.

In experiments with tropomyosin or fimbrin, actin filaments ($C_{G\text{-}actin}$ = 1 µM) were incubated with tropomyosin at a 1:3 protein concentration ratio or with fimbrin at a 3:2 protein concentration ratio for 15 min prior to addition to the SLB (Palani et al., 2019).

In experiments with muscle myosin II filaments, we prepared muscle myosin II filaments by diluting the stock of muscle myosin II proteins (rabbit, m. psoas, cat. no. 8326-01, Hypermol) (C_{myoII} = 20 µM; 500mM KCl, 1mM EDTA, 1 mM DTT, 10 mM HEPES, pH 7.0) 10-times with MilliQ water to drop the KCl concentration to 50 mM and incubated for 5 min to ensure myosin filament formation. Myosin II filaments were further diluted in KMEH to 200 nM and added to the actin filaments bound to the SLB by His_6-Curly by replacing 1/10 of the sample buffer with the myosin II filament solution and supplemented with 0.1 mM Mg-ATP as well as a mix of 1 mM Trolox (cat. no. 648471, Merck), 2 mM protocatechuic acid (cat. no.

bioRxiv preprint doi: https://doi.org/10.1101/2020.07.10.197616; this version posted July 14, 2020. The copyright holder for this preprint (which was not certified by peer review) is the author/funder, who has granted bioRxiv a license to display the preprint in perpetuity. It is made available under aCC-BY 4.0 International license.

03930590, Merck) and 0.1 µM protocatechuate 3,4-dioxygenase (cat. no. P8279, Merck) to minimize photobleaching. To summarize, the final buffer composition was 50mM KCl, 2mM $MgCl_2$, 1mM EGTA, 20mM HEPES, 0.1mM ATP, 1 mM Trolox, 2 mM protocatechuic acid and 0.1 µM protocatechuate 3,4-dioxygenase at pH 7.2 containing actin filaments ($C_{G\text{-}actin}$ = 100 nM) and myosin II filaments (C_{myoII} = 20 nM). It was important to keep the pH at 7.2, as changes in pH would affect motor activity. As reported earlier, myosin filaments started to show actin network remodeling activity after about 10-15 min of incubation (Köster et al., 2016; Mosby et al., 2020).

TIRF microscopy

Images were acquired using a Nikon Eclipse Ti-E/B microscope equipped with perfect focus system, a Ti-E TIRF illuminator (CW laser lines: 488nm, 561nm and 640nm) and a Zyla sCMOS 4.2 camera (Andor, Oxford Instruments, UK) controlled by Andor iQ3 software (https://andor.oxinst.com/products/iq-live-cell-imaging-software/).

Image analysis

Images were analyzed using ImageJ (http://imagej.nih.gov/ij).
Curvature was measured by fitting ellipses to match the actin filament contour by hand, while measuring first fully formed rings before curved actin filament segments and by going from the highest curvatures down to lower curvatures in each image with a cut off for measurements at curvatures smaller than 0.1 μm^{-1} or at 30-40 measurements per image (see examples in Figure 1 – figure supplement 1D; Figure 1-figure supplement 2B).
To measure the angle of kinks in individual actin filaments, cropped images of individual actin filaments were processed with a Sobel filter (part of the Mosaic suit for ImageJ, http://mosaic.mpi-cbg.de/?q=downloads/imageJ) to highlight the actin filament center, and the angles were measured manually with the ImageJ angle tool.
The actin ring contraction rate upon myosin II filament action was measured by generating kymographs based on a line (3 pixels width) dividing the ring into two equal halves.

Data plotting and statistics

Graphs were generated using OriginPro (version 2019b, OriginLab, USA). Plots depict individual data points, mean (circle), median (central line) and standard deviation (top and bottom lines).

Acknowledgement

The authors would like to thank Dr. Gayathri Panaghat (IISER Pune, India), Dr. Minhaj Sirajuddin (InStem, Bangalore, India), for insightful discussions and Prof. Gijsje Koenderink (TU Delft, Netherlands) and Prof. Rob Cross (University of Warwick, UK) for helpful comments on the manuscript. The work was supported by a Wellcome Investigator Award (WT 101885MA) and an ERC advanced grant (ERC-2014-ADG N° 671083) to MKB. DVK thanks the Wellcome-Warwick Quantitative Biomedicine Programme for funding (RMRCB0058).

Competing Interests

The authors have no competing interests to declare.

References

Almonacid, M., Celton-Morizur, S., Jakubowski, J. L., Dingli, F., Loew, D., Mayeux, A., Chen, J. S., Gould, K. L., Clifford, D. M., & Paoletti, A. (2011). Temporal control of contractile ring assembly by Plo1 regulation of myosin II recruitment by Mid1/anillin. *Current Biology*, *21*(6), 473–479. https://doi.org/10.1016/j.cub.2011.02.003

Bieling, P., Li, T.-D., Weichsel, J., McGorty, R., Jreij, P., Huang, B., Fletcher, D. A., & Mullins, R. D. (2016). Force Feedback Controls Motor Activity and Mechanical Properties of Self-Assembling Branched Actin Networks. *Cell*, *164*(1–2), 115–127. https://doi.org/10.1016/j.cell.2015.11.057

Briggs, M. W., & Sacks, D. B. (2003). IQGAP proteins are integral components of

bioRxiv preprint doi: https://doi.org/10.1101/2020.07.10.197616; this version posted July 14, 2020. The copyright holder for this preprint (which was not certified by peer review) is the author/funder, who has granted bioRxiv a license to display the preprint in perpetuity. It is made available under aCC-BY 4.0 International license.

cytoskeletal regulation. *EMBO Reports*, *4*(6), 571–574. https://doi.org/10.1038/sj.embor.embor867

De La Cruz, E. M., & Gardel, M. L. (2015). Actin mechanics and fragmentation. *Journal of Biological Chemistry*, *290*(28), 17137–17144. https://doi.org/10.1074/jbc.R115.636472

Eng, K., Naqvi, N. I., Wong, K. C. Y., & Balasubramanian, M. K. (1998). Rng2p, a protein required for cytokinesis in fission yeast, is a component of the actomyosin ring and the spindle pole body. *Current Biology*, *8*(11), 611–621. https://doi.org/10.1016/S0960-9822(98)70248-9

Epp, J. A., & Chant, J. (1997). An IQGAP-related protein controls actin-ring formation and cytokinesis in yeast. *Current Biology*, *7*(12), 921–929. https://doi.org/10.1016/S0960-9822(06)00411-8

Hayakawa, Y., Takaine, M., Imai, T., Yamada, M., Hirose, K., Tokuraku, K., Ngo, K. X., Kodera, N., Numata, O., Nakano, K., & Uyeda, T. Q. P. (2020). Actin binding domain of Rng2 strongly inhibits actin movement on myosin II HMM through structural changes of actin filaments. *BioarXiv*.

Köster, D. V., Husain, K., Iljazi, E., Bhat, A., Bieling, P., Mullins, R. D., Rao, M., & Mayor, S. (2016). Actomyosin dynamics drive local membrane component organization in an in vitro active composite layer. *Proceedings of the National Academy of Sciences*, *113*(12), E1645–E1654. https://doi.org/10.1073/pnas.1514030113

Kruppa, A. J., Kishi-Itakura, C., Masters, T. A., Rorbach, J. E., Grice, G. L., Kendrick-Jones, J., Nathan, J. A., Minczuk, M., & Buss, F. (2018). Myosin VI-Dependent Actin Cages Encapsulate Parkin-Positive Damaged Mitochondria. *Developmental Cell*, *44*(4), 484-499.e6. https://doi.org/10.1016/j.devcel.2018.01.007

Kučera, O., Janda, D., Siahaan, V., Dijkstra, S. H., Pilátová, E., Zatecka, E., Diez, S., Braun, M., & Lansky, Z. (2020). Anillin propels myosin-independent constriction of actin rings. *BioRxiv*, 1–27. https://doi.org/10.1101/2020.01.22.915256

Kumari, A., Kesarwani, S., Javoor, M. G., Vinothkumar, K. R., & Sirajuddin, M. (2020). Structural insights into actin filament recognition by commonly used cellular actin markers. *The EMBO Journal*, 846337. https://doi.org/10.15252/embj.2019104006

Laplante, C., Huang, F., Tebbs, I. R., Bewersdorf, J., & Pollard, T. D. (2016). Molecular organization of cytokinesis nodes and contractile rings by super-resolution fluorescence microscopy of live fission yeast. *Proceedings of the National Academy of Sciences*, *113*(40), E5876–E5885. https://doi.org/10.1073/pnas.1608252113

Laporte, D., Coffman, V. C., Lee, I. J., & Wu, J. Q. (2011). Assembly and architecture of precursor nodes during fission yeast cytokinesis. *Journal of Cell Biology*, *192*(6), 1005–1021. https://doi.org/10.1083/jcb.201008171

Li, Y., & Munro, E. (2020). Existing actin filaments orient new filament growth to provide structural memory of filament alignment during cytokinesis. *BioRxiv*. https://doi.org/10.1101/2020.04.13.039586

Litschel, T., Kelley, C. F., Holz, D., Koudehi, M. A., Vogel, S. K., Burbaum, L., Mizuno, N., Vavylonis, D., & Schwille, P. (2020). Reconstitution of contractile actomyosin rings in vesicles. *BioRxiv*. https://doi.org/10.1101/2020.06.30.180901

Mavrakis, M., Azou-Gros, Y., Tsai, F.-C., Alvarado, J., Bertin, A., Iv, F., Kress, A., Brasselet, S., Koenderink, G. H., & Lecuit, T. (2014). Septins promote F-actin ring formation by crosslinking actin filaments into curved bundles. *Nature Cell Biology*, *16*(4), 322–334. https://doi.org/10.1038/ncb2921

Mishra, M., Kashiwazaki, J., Takagi, T., Srinivasan, R., Huang, Y., Balasubramanian, M. K., & Mabuchi, I. (2013). In vitro contraction of cytokinetic ring depends on myosin II but not on actin dynamics. *Nature Cell Biology*, *15*(7), 853–859. https://doi.org/10.1038/ncb2781

Mosby, L. S., Hundt, N., Young, G., Fineberg, A., Polin, M., Mayor, S., Kukura, P., & Köster, D. V. (2020). Myosin II Filament Dynamics in Actin Networks Revealed with Interferometric Scattering Microscopy. *Biophysical Journal*, *118*(8), 1946–1957. https://doi.org/10.1016/j.bpj.2020.02.025

Murrell, M. P., & Gardel, M. L. (2012). F-actin buckling coordinates contractility and severing in a biomimetic actomyosin cortex. *Proceedings of the National Academy of Sciences of the United States of America*, *19*. https://doi.org/10.1073/pnas.1214753109

Narita, A. (2020). ADF/cofilin regulation from a structural viewpoint. *Journal of Muscle*

bioRxiv preprint doi: https://doi.org/10.1101/2020.07.10.197616; this version posted July 14, 2020. The copyright holder for this preprint (which was not certified by peer review) is the author/funder, who has granted bioRxiv a license to display the preprint in perpetuity. It is made available under aCC-BY 4.0 International license.

Research and Cell Motility, *41*(1), 141–151. https://doi.org/10.1007/s10974-019-09546-6

Nye, J. A., & Groves, J. T. (2008). Kinetic control of histidine-tagged protein surface density on supported lipid bilayers. *Langmuir : The ACS Journal of Surfaces and Colloids*, *24*(8), 4145–4149. https://doi.org/10.1021/la703788h

Padmanabhan, A., Bakka, K., Sevugan, M., Naqvi, N. I., D'Souza, V., Tang, X., Mishra, M., & Balasubramanian, M. K. (2011). IQGAP-related Rng2p organizes cortical nodes and ensures position of cell division in fission yeast. *Current Biology*, *21*(6), 467–472. https://doi.org/10.1016/j.cub.2011.01.059

Palani, S., Köster, D. V., Hatano, T., Kamnev, A., Kanamaru, T., Brooker, H. R., Hernandez-Fernaud, J. R., Jones, A. M. E., Millar, J. B. A., Mulvihill, D. P., & Balasubramanian, M. K. (2019). Phosphoregulation of tropomyosin is crucial for actin cable turnover and division site placement. *The Journal of Cell Biology*, jcb.201809089. https://doi.org/10.1083/jcb.201809089

Pardee, J. D., & Spudich, J. A. (1982). Purification of muscle actin. *Methods in Cell Biology*, *24*, 271–289. http://www.ncbi.nlm.nih.gov/pubmed/7098993

Skau, C. T., & Kovar, D. R. (2010). Fimbrin and tropomyosin competition regulates endocytosis and cytokinesis kinetics in fission yeast. *Current Biology*, *20*(16), 1415–1422. https://doi.org/10.1016/j.cub.2010.06.020

Skoumpla, K., Coulton, A. T., Lehman, W., Geeves, M. A., & Mulvihill, D. P. (2007). Acetylation regulates tropomyosin function in the fission yeast Schizosaccharomyces pombe. *Journal of Cell Science*, *120*(9), 1635–1645. https://doi.org/10.1242/jcs.001115

Swulius, M. T., Nguyen, L. T., Ladinsky, M. S., Ortega, D. R., Aich, S., Mishra, M., & Jensen, G. J. (2018). Structure of the fission yeast actomyosin ring during constriction. *Proceedings of the National Academy of Sciences of the United States of America*, *115*(7), E1455–E1464. https://doi.org/10.1073/pnas.1711218115

Taylor, K. A., Taylor, D. W., & Schachat, F. (2000). Isoforms of α-actinin from cardiac, smooth, and skeletal muscle form polar arrays of actin filaments. *Journal of Cell Biology*, *149*(3), 635–645. https://doi.org/10.1083/jcb.149.3.635

Tebbs, I. R., Pollard, T. D., & D, P. T. (2013). Separate roles of IQGAP Rng2p in forming and constricting the Schizosaccharomyces pombe cytokinetic contractile ring. *Molecular Biology of the Cell*, *24*(12), 1904–1917. https://doi.org/10.1091/mbc.E12-10-0775

Toyoshima, Y. Y., Kron, S. J., & Spudicht, J. A. (1990). The myosin step size: Measurement of the unit displacement per ATP hydrolyzed in an in vitro assay (actin/crossbridge/muscle contraction). In *Proc. Nati. Acad. Sci. USA* (Vol. 87, Issue September).

Vassilopoulos, S., Gibaud, S., Jimenez, A., Caillol, G., & Leterrier, C. (2019). Ultrastructure of the axonal periodic scaffold reveals a braid-like organization of actin rings. *Nature Communications*, *10*(1), 636217. https://doi.org/10.1038/s41467-019-13835-6

Wang, C.-H., Balasubramanian, M. K., & Dokland, T. (2004). Structure, crystal packing and molecular dynamics of the calponin-homology domain of Schizosaccharomyces pombe Rng2. *Acta Crystallographica Section D Biological Crystallography*, *60*(8), 1396–1403. https://doi.org/10.1107/S0907444904012983

Way, M., Sanders, M., Garcia, C., Sakai, J., & Matsudaira, P. (1995). Sequence and domain organization of scruin, an actin-cross-linking protein in the acrosomal process of Limulus sperm. *Journal of Cell Biology*, *128*(1–2), 51–60.

Xu, K., Zhong, G., & Zhuang, X. (2013). Actin, spectrin, and associated proteins form a periodic cytoskeletal structure in axons. *Science (New York, N.Y.)*, *339*(6118), 452–456. https://doi.org/10.1126/science.1232251

bioRxiv preprint doi: https://doi.org/10.1101/2020.07.10.197616; this version posted July 14, 2020. The copyright holder for this preprint (which was not certified by peer review) is the author/funder, who has granted bioRxiv a license to display the preprint in perpetuity. It is made available under aCC-BY 4.0 International license.

Figure 1

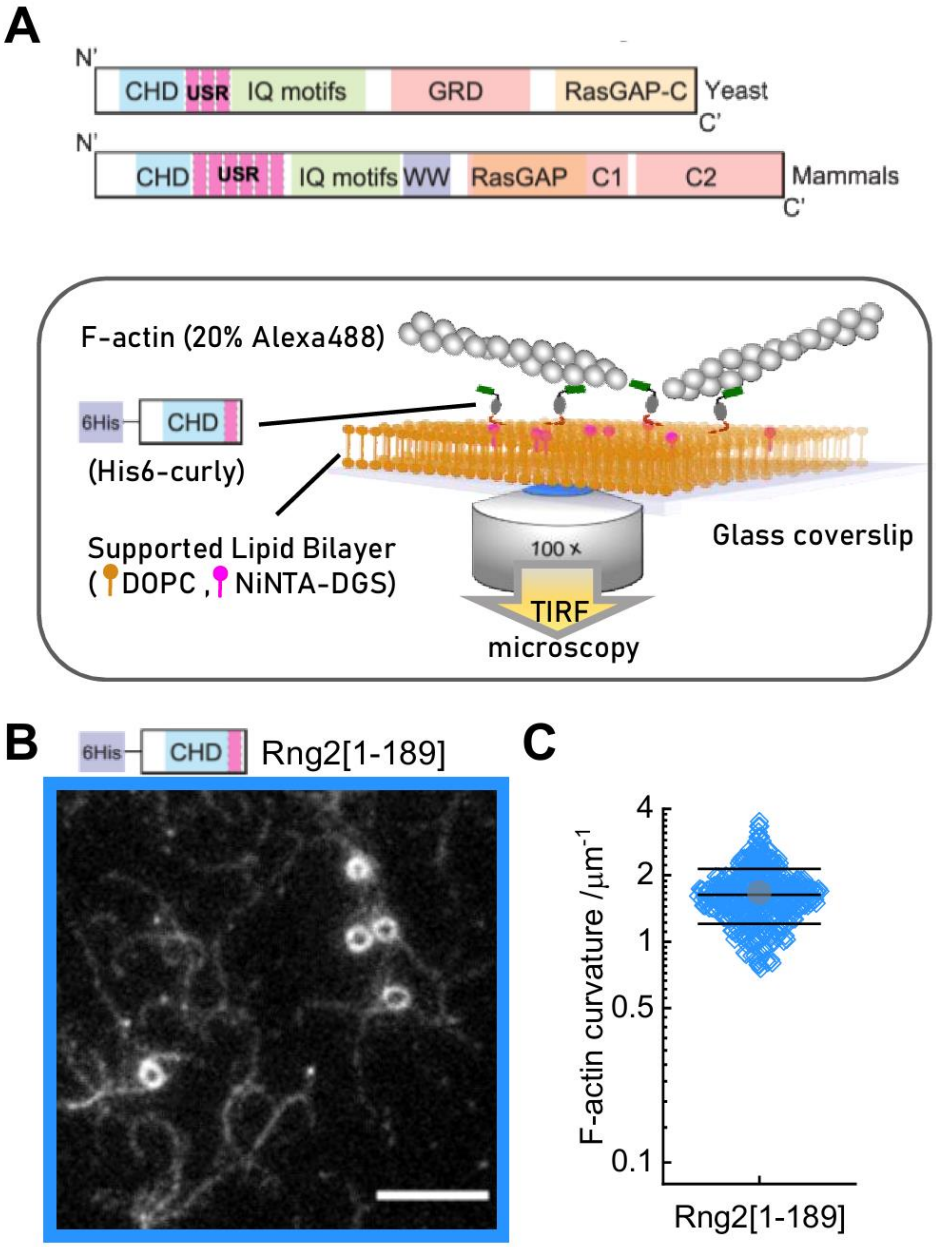

Figure 1 – Formation of actin filament rings by membrane tethered curly (Rng2[1-189])

(A) Schematic representation of (top) the IQGAP proteins Rng2 (yeast, *S. pombe*) and IQGAP1 (mammals, *H. Sapiens*) and (bottom) the experimental setup used in this study; CHD - Calponin Homology Domain, USR – Unstructured Region, GRD - GAP Related Domain, RasGAP – Ras GTPase Activating Protein, WW – tryptophan containing protein domain.

(B) TIRF microscopy image of actin filaments (Alexa488) bound to SLB tethered His_6-curly; scale bar 5 µm.

(C) Curvature measurements of actin filament rings and curved segments; shown are the individual data points and their mean ± s.d.; N = 425 obtained from 8 field of views from 4 individual experiments.

bioRxiv preprint doi: https://doi.org/10.1101/2020.07.10.197616; this version posted July 14, 2020. The copyright holder for this preprint (which was not certified by peer review) is the author/funder, who has granted bioRxiv a license to display the preprint in perpetuity. It is made available under aCC-BY 4.0 International license.

Figure 1 - figure supplement 1

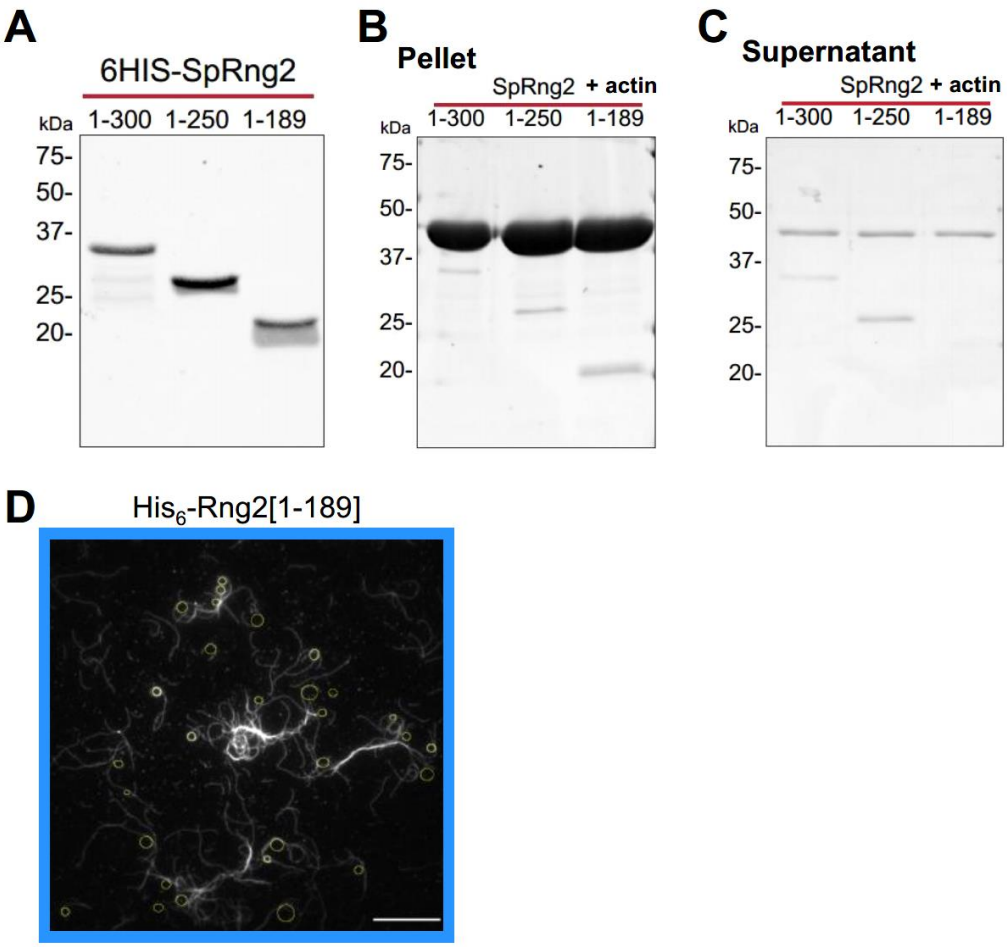

Figure 1 – figure supplement 1

(A) Western blot of the different His_6-Rng2 constructs after protein purification.

(B) SDS-PAGE of the actin filament pellet after incubation with His_6-Rng2 constructs and centrifugation at 100,000g for 20 min at 25°C.

(C) SDS-PAGE of the supernatant from the sample described in (B).

(D) TIRF microscopy image of actin filaments (Alexa488) bound to SLB tethered His_6- curly; circles show curvature measurements; scale bar 10 µm.

bioRxiv preprint doi: https://doi.org/10.1101/2020.07.10.197616; this version posted July 14, 2020. The copyright holder for this preprint (which was not certified by peer review) is the author/funder, who has granted bioRxiv a license to display the preprint in perpetuity. It is made available under aCC-BY 4.0 International license.

Figure 1 - figure supplement 2

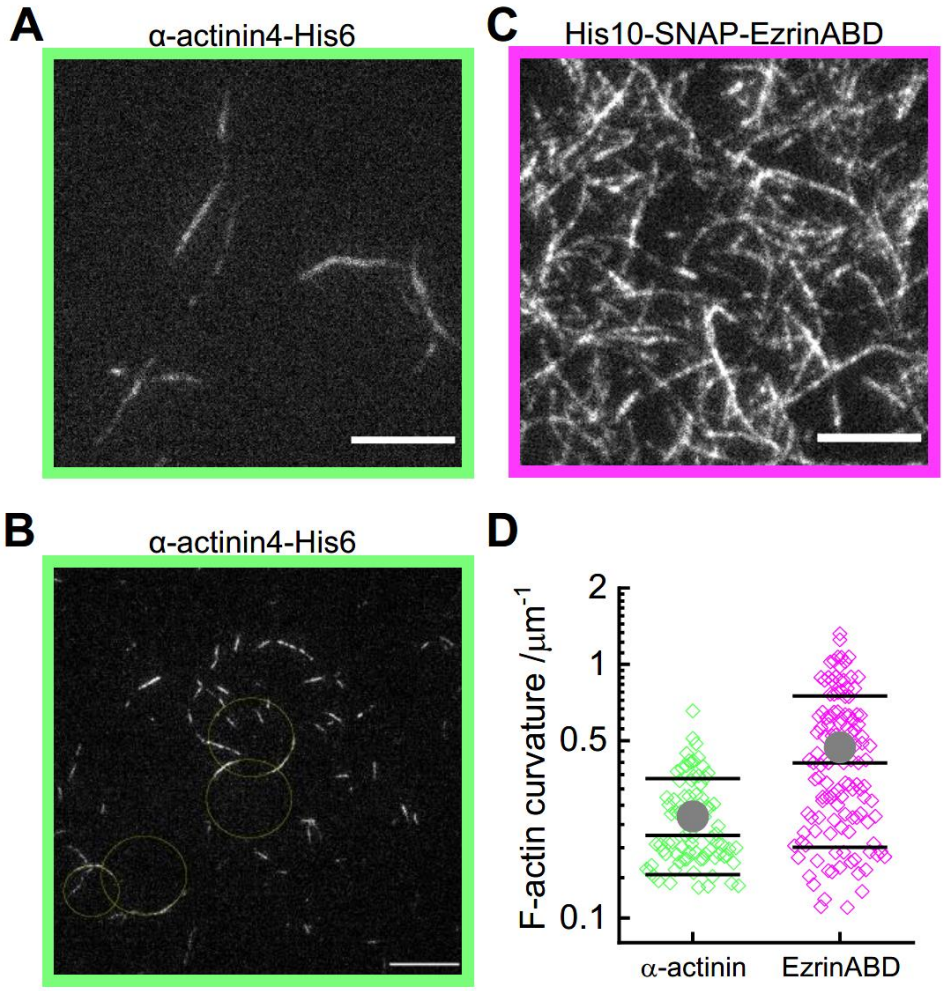

Figure 1-figure supplement 2

(A) TIRF microscopy image of actin filaments (Alexa488) bound to SLB tethered α-actinin-His_6; scale bar 5 μm.

(B) TIRF microscopy image of actin filaments (Alexa488) bound to SLB tethered α-actinin-His_6; circles show curvature measurements; scale bar 10 μm.

(C) TIRF microscopy image of actin filaments (Alexa488) bound to SLB tethered His_{10}-EzrinABD; scale bar 5 μm.

(D) Curvature measurements of actin filament rings and curved segments; shown are the individual data points and their mean ± s.d.; α-actinin-His_6 : N = 85 obtained from 10 field of views from 4 individual experiments; His_{10}-EzrinABD : N = 127 obtained from 9 field of views from 3 individual experiments.

bioRxiv preprint doi: https://doi.org/10.1101/2020.07.10.197616; this version posted July 14, 2020. The copyright holder for this preprint (which was not certified by peer review) is the author/funder, who has granted bioRxiv a license to display the preprint in perpetuity. It is made available under aCC-BY 4.0 International license.

Figure 2

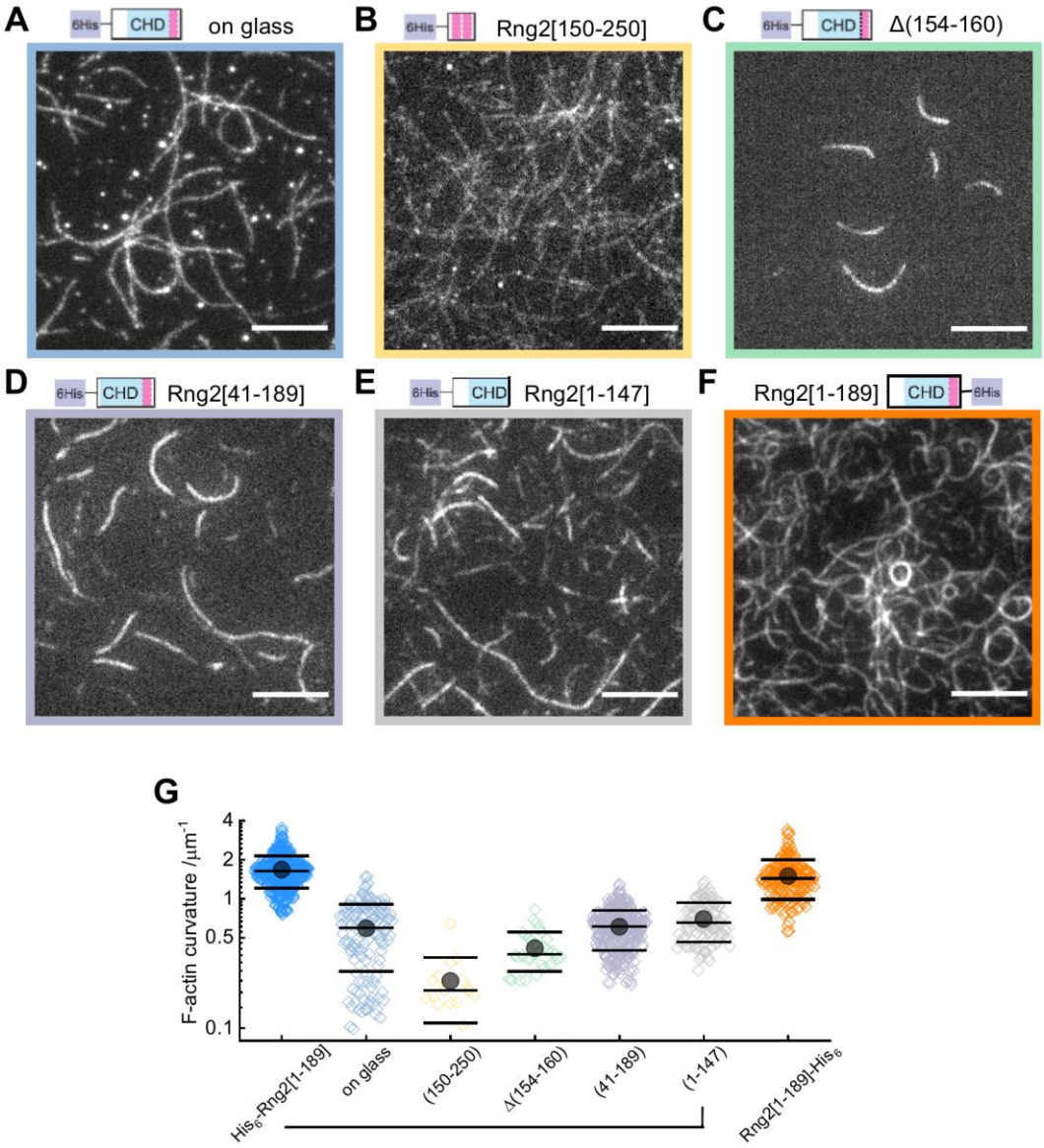

Figure 2 – Characterization of actin binding and bending by fragments of curly
TIRF microscopy images of actin filaments (Alexa488) bound to

(A) glass adsorbed His6-curly; N = 138 from 9 field of views from 3 independent experiments;
(B) SLB bound His_6-Rng2[150-250]; N = 144 from 10 field of views from 2 independent experiments;
(C) SLB bound His_6-Rng2[1-189]Δ(154-160); N = 33 from 10 field of views from 2 independent experiments;
(D) SLB bound His_6-Rng2[41-189]; N = 323 from 9 field of views from 3 independent experiments;
(E) SLB bound His_6-Rng2[1-147]; N = 118 from 12 field of views from 2 experiments;
(F) SLB bound Rng2[1-189]-His_6; N = 658 from 16 field of views from 4 experiments; Scale bars: 5 µm.
(G) Curvature measurements of actin filament rings and curved segments; shown are the individual data points and their mean ± s.d.

bioRxiv preprint doi: https://doi.org/10.1101/2020.07.10.197616; this version posted July 14, 2020. The copyright holder for this preprint (which was not certified by peer review) is the author/funder, who has granted bioRxiv a license to display the preprint in perpetuity. It is made available under aCC-BY 4.0 International license.

Figure 2 - figure supplement 1

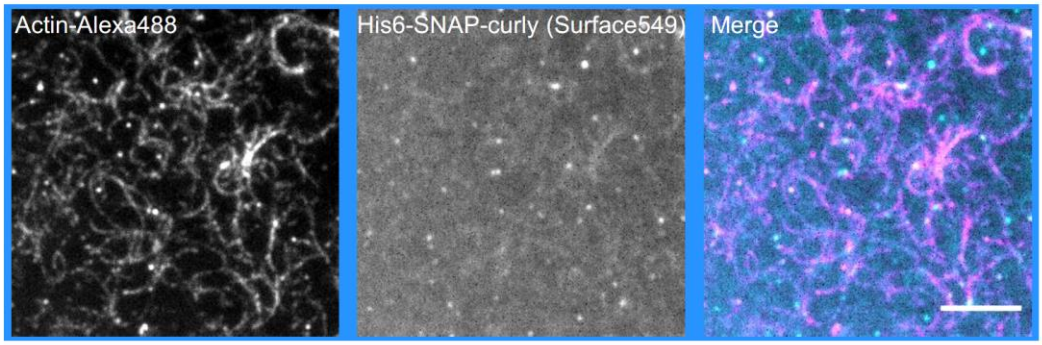

Figure 2- supplement figure 1

Dual color TIRF microscopy image of actin filaments (Alexa488, magenta) bound to SLB tethered fluorescently labelled His_6-SNAP-curly (Surface549, cyan); scale bar 5 µm.

bioRxiv preprint doi: https://doi.org/10.1101/2020.07.10.197616; this version posted July 14, 2020. The copyright holder for this preprint (which was not certified by peer review) is the author/funder, who has granted bioRxiv a license to display the preprint in perpetuity. It is made available under aCC-BY 4.0 International license.

Figure 2 - figure supplement 2

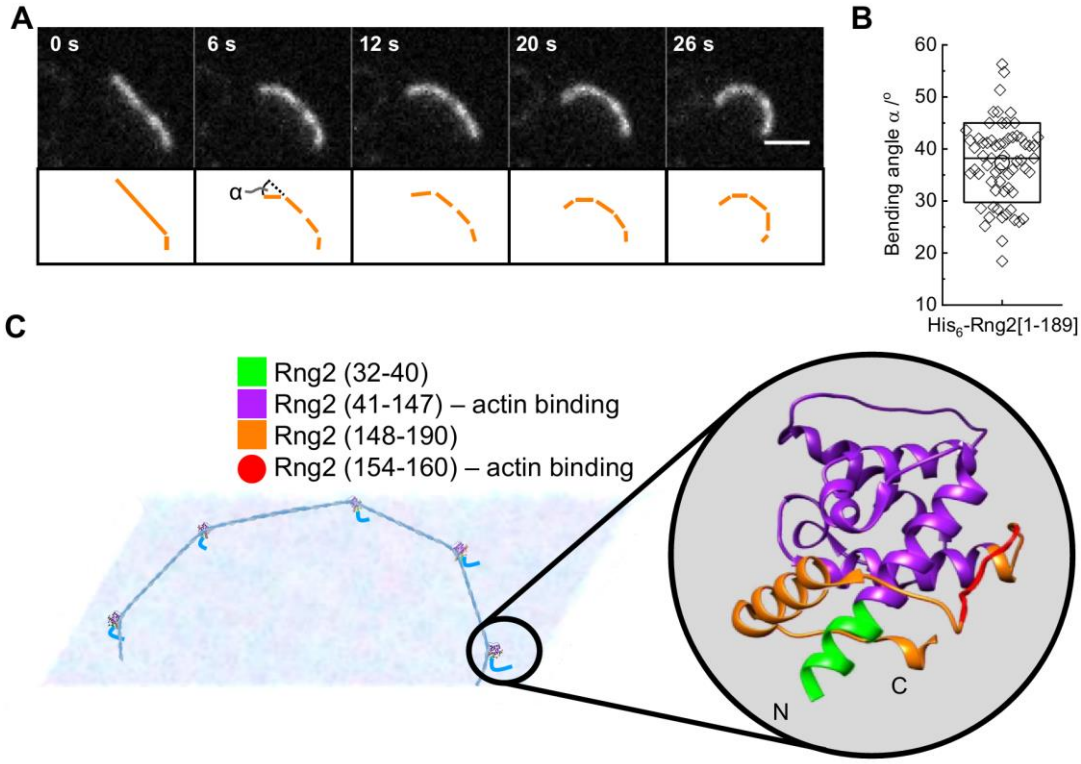

Figure 2- supplement figure 2

(A) TIRF microscopy image time series of an actin filament (Alexa488) bound to SLB tethered His_6-curly and displaying stepwise bending; scale bar: 1 µm.

(B) Bending angles of individual bending events in actin filaments; shown are the individual data points and their mean ± s.d.; N = 63 from 6 individual actin filaments.

(C) Model representation of curly and how it could interact with actin to induce local bends in the actin filament; the inlet shows curly with the regions tested in this study highlighted in color.

bioRxiv preprint doi: https://doi.org/10.1101/2020.07.10.197616; this version posted July 14, 2020. The copyright holder for this preprint (which was not certified by peer review) is the author/funder, who has granted bioRxiv a license to display the preprint in perpetuity. It is made available under aCC-BY 4.0 International license.

Figure 3

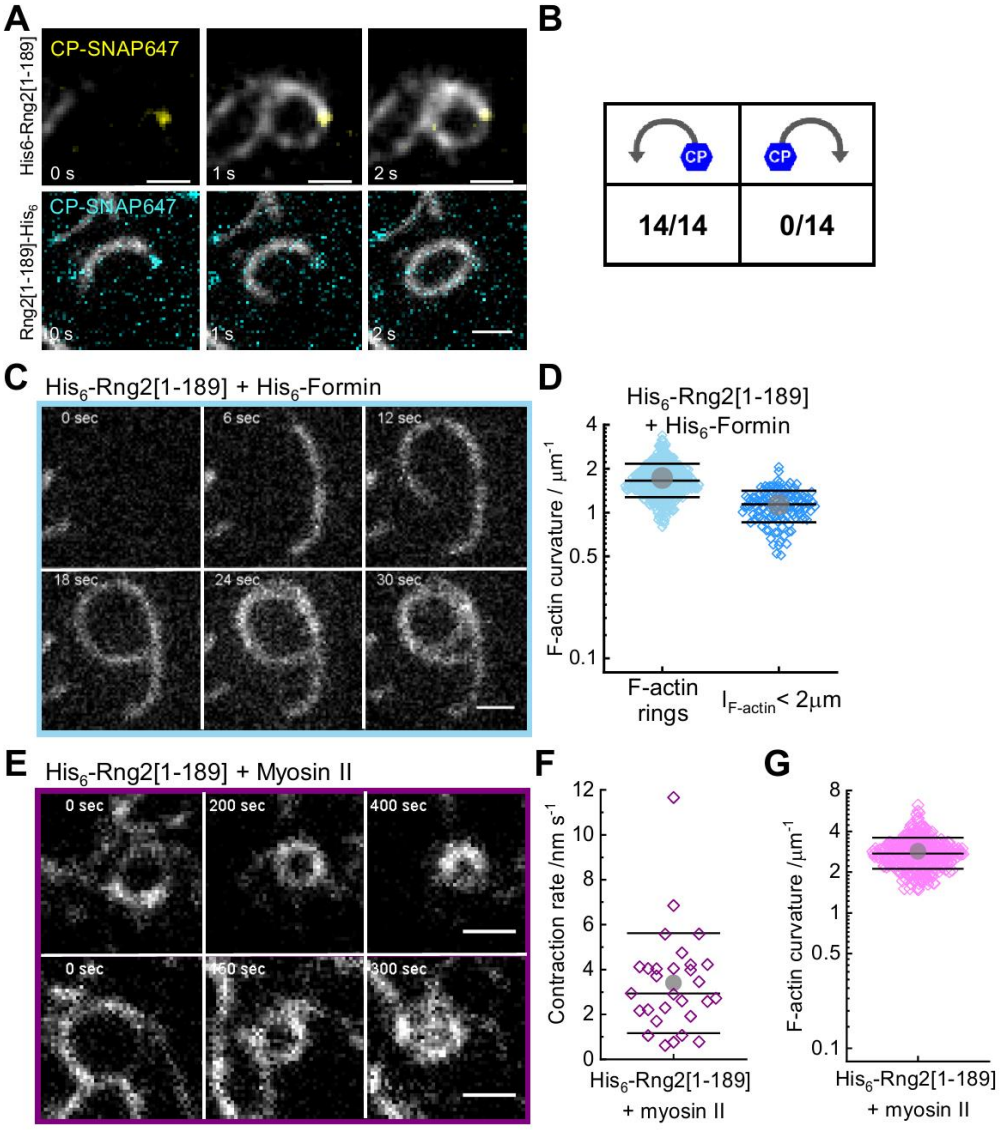

Figure 3 – Curly recognizes actin filament orientation and enables actin ring contraction by myosin II

(A) TIRF microscopy images of actin filaments (Alexa488) with the plus end marked with SNAP647-tagged capping protein binding to His_6-curly (top) and curly-His_6 (bottom); scale bar: 1 µm.

(B) Count of actin filament bending orientations with respect to the capping protein where individual actin filaments could be identified.

(C) TIRF microscopy images of a polymerizing actin filament (Alexa488) driven by membrane tethered His_6-formin in the presence of His_6-curly; scale bar: 1 µm.

(D) Curvature measurements of actin filament rings (light blue) and curved short actin filaments (< 2 µm; dark blue); shown are the individual data points and their mean ± s.d.; N_{rings} = 477, N_{short} = 125 from 9 field of views of 3 independent experiments.

(E) TIRF microscopy images of actin filament (Alexa488) ring contraction after addition of muscle myosin II filaments on His_6-curly containing SLBs; scale bar: 1 µm.

(F) Average contraction rates of actin filament rings after addition of muscle myosin II filaments; shown are the individual data points and their mean ± s.d.; N = 18 from 2 individual experiments.

(G) Curvature measurements of actin filament rings and curved segments 20 min after addition of myosin II filaments; shown are the individual data points and their mean ± s.d.; N = 342 from 10 field of views of 2 individual experiments.

bioRxiv preprint doi: https://doi.org/10.1101/2020.07.10.197616; this version posted July 14, 2020. The copyright holder for this preprint (which was not certified by peer review) is the author/funder, who has granted bioRxiv a license to display the preprint in perpetuity. It is made available under aCC-BY 4.0 International license.

Figure 3 - figure supplement 1

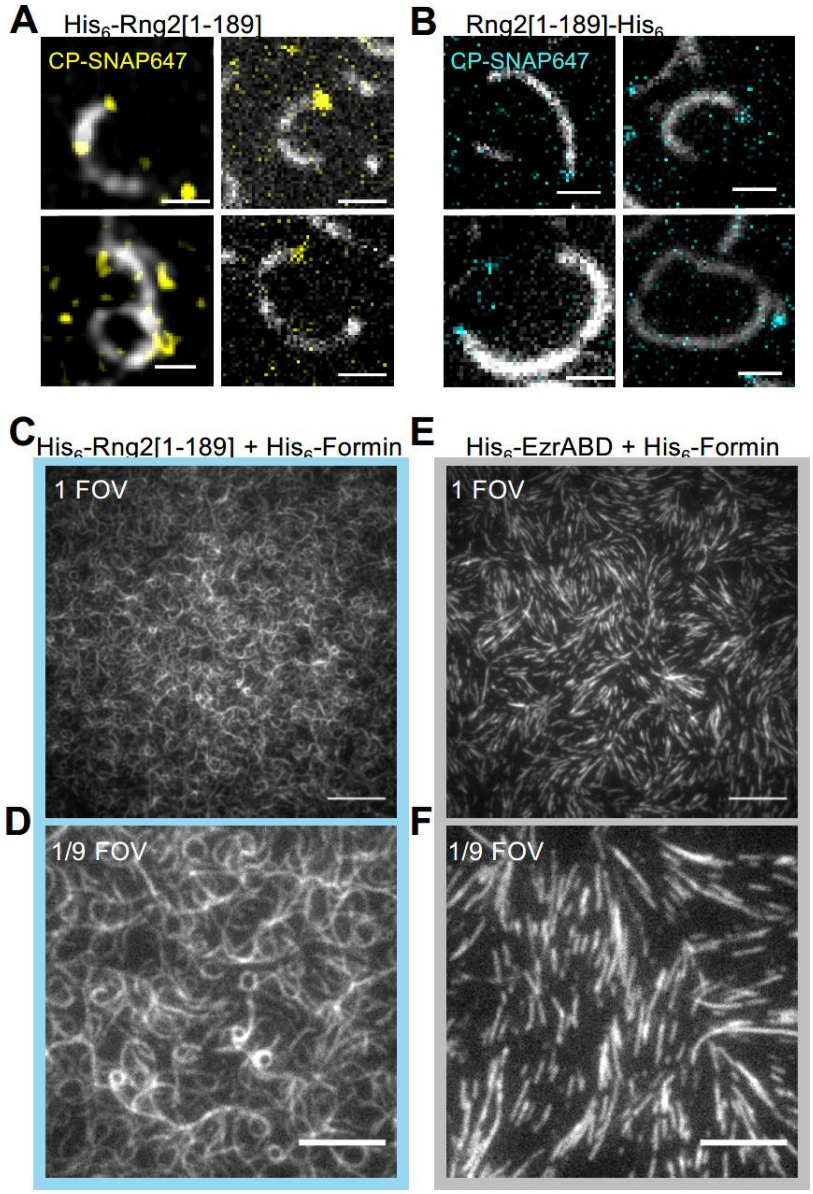

Figure 3-figure supplement 1

(A) TIRF microscopy images of actin filaments (Alexa488) with the plus end marked with SNAP647-tagged capping protein binding to His_6-curly; scale bar: 1 µm.

(B) TIRF microscopy images of actin filaments (Alexa488) with the plus end marked with SNAP647-tagged capping protein binding to curly- His_6; scale bar: 1 µm.

(C) TIRF microscopy image (representing one field of view) of actin filaments (Alexa488) polymerized by membrane tethered His_6-formin in the presence of His_6-curly; scale bar: 10 µm.

(D) TIRF microscopy image (representing 1/9 of the field of view) of actin filaments (Alexa488) polymerized by membrane tethered His_6-formin in the presence of His_6-curly; scale bar: 5 µm.

(E) TIRF microscopy image (representing one field of view) of actin filaments (Alexa488) polymerized by membrane tethered His_6-formin in the presence of His_{10}-EzrinABD; scale bar: 10 µm.

(F) TIRF microscopy image (representing 1/9 of the field of view) of actin filaments (Alexa488) polymerized by membrane tethered His_6-formin in the presence of His_{10}-EzrinABD; scale bar: 5 µm.

bioRxiv preprint doi: https://doi.org/10.1101/2020.07.10.197616; this version posted July 14, 2020. The copyright holder for this preprint (which was not certified by peer review) is the author/funder, who has granted bioRxiv a license to display the preprint in perpetuity. It is made available under aCC-BY 4.0 International license.

Figure 3 - figure supplement 2

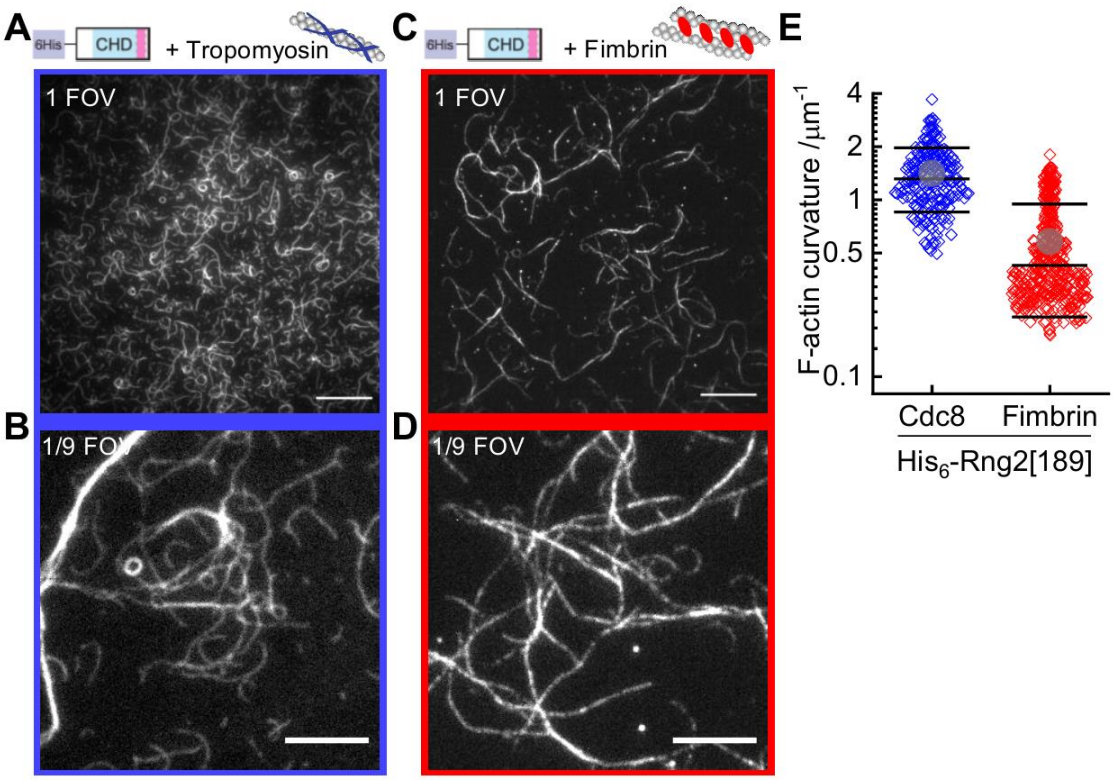

Figure 3-figure supplement 2

(A) TIRF microscopy image (representing one field of view) of actin filaments (Alexa488) pre-incubated with tropomyosin (Cdc8) bound to membrane tethered His_6-curly; scale bar: 10 µm.

(B) TIRF microscopy image (representing 1/9 field of view) of actin filaments (Alexa488) pre-incubated with tropomyosin (Cdc8) bound to membrane tethered His_6-curly; scale bar: 5 µm.

(C) TIRF microscopy image (representing one field of view) of actin filaments (Alexa488) pre-incubated with fimbrin bound to membrane tethered His_6-curly; scale bar: 10 µm.

(D) TIRF microscopy image (representing 1/9 field of view) of actin filaments (Alexa488) pre-incubated with fimbrin bound to membrane tethered His_6-curly; scale bar: 5 µm.

(E) Curvature measurements of actin filament rings and curved segments; shown are the individual data points and their mean ± s.d.; tropomyosin (Cdc8, blue): N = 204 from 9 field of views of 3 individual experiments; fimbrin (red): N = 407 from 20 field of views of 3 individual experiments.

bioRxiv preprint doi: https://doi.org/10.1101/2020.07.10.197616; this version posted July 14, 2020. The copyright holder for this preprint (which was not certified by peer review) is the author/funder, who has granted bioRxiv a license to display the preprint in perpetuity. It is made available under aCC-BY 4.0 International license.

Figure 3 - figure supplement 3

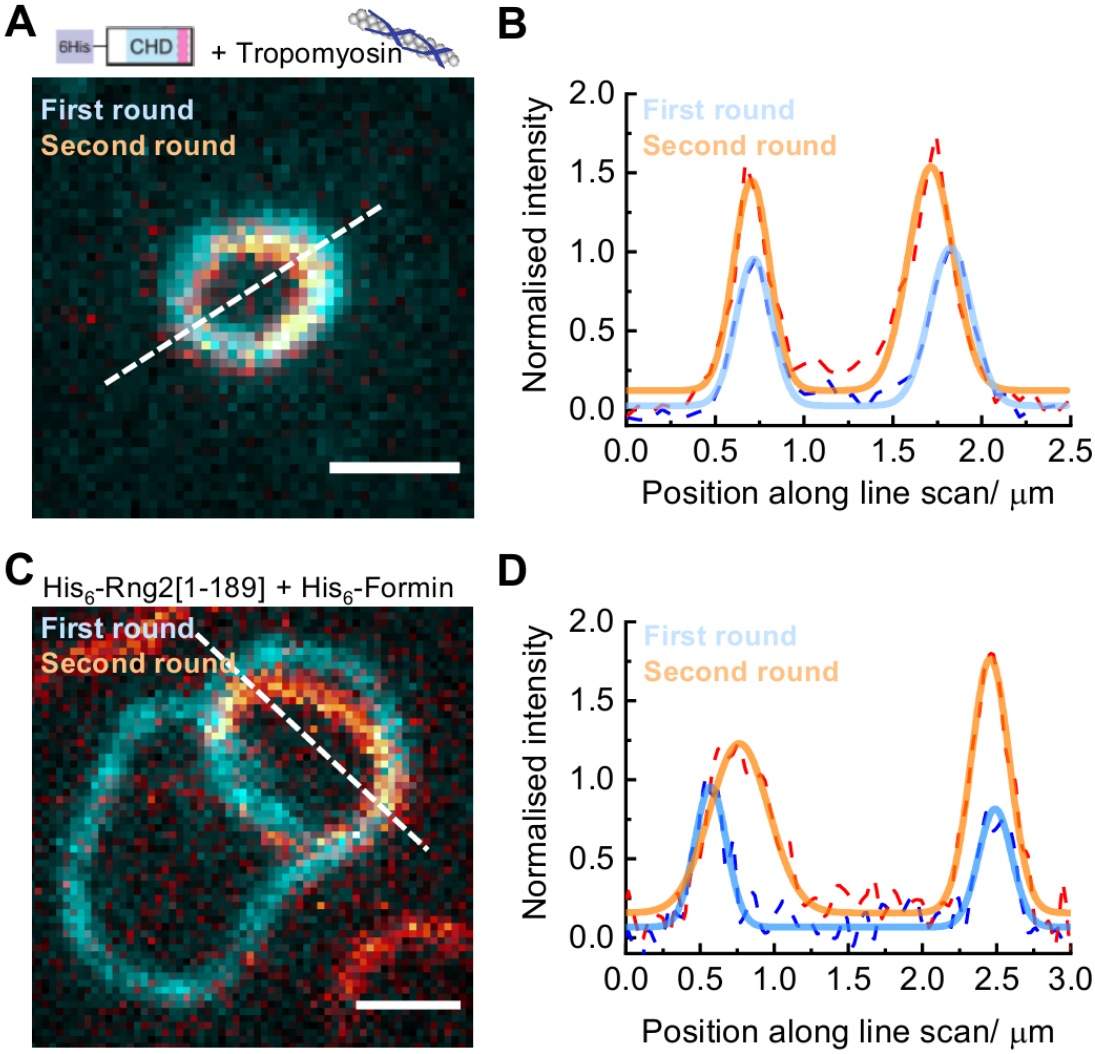

Figure 3-figure supplement 3

(A) TIRF microscopy image overlay showing multiple ring formation of a tropomyosin coated actin filament (Alexa488) during binding to membrane tethered His_6-curly; the first ring formed is colored in cyan, the second ring (in orange) was highlighted by subtracting the image of the first ring from the image stack; scale bar: 1 µm.

(B) Intensity line scan (3 pixels width) along the dashed line in (A) and corresponding Gaussian peak fits.

(C) TIRF microscopy image overlay showing multiple ring formation of a polymerizing actin filament (Alexa488) by membrane tethered His_6-formin in presence of membrane tethered His_6-curly; the first ring formed is colored in cyan, the second ring (in orange) was highlighted by subtracting the image of the first ring from the image stack; scale bar: 1 µm.

(D) Intensity line scan (3 pixels width) along the dashed line in (C) and corresponding Gaussian peak fits.

bioRxiv preprint doi: https://doi.org/10.1101/2020.07.10.197616; this version posted July 14, 2020. The copyright holder for this preprint (which was not certified by peer review) is the author/funder, who has granted bioRxiv a license to display the preprint in perpetuity. It is made available under aCC-BY 4.0 International license.

Figure 3 - figure supplement 4

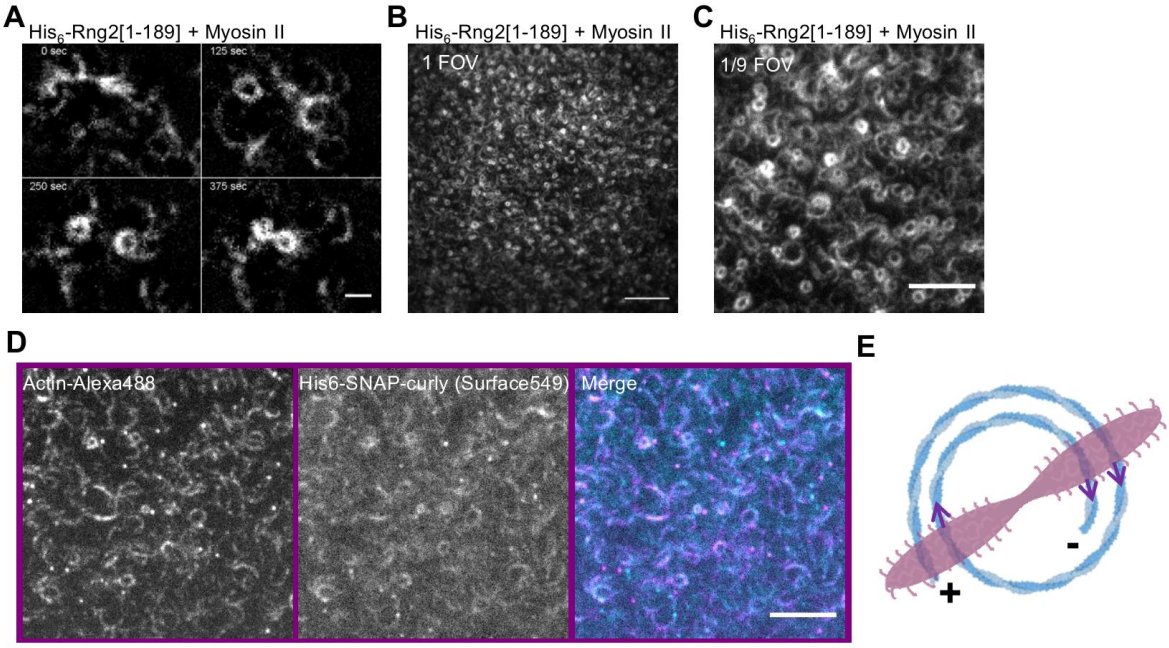

Figure 3-figure supplement 4

(A) TIRF microscopy image time series showing actin filament (Alexa488) ring formation, translation and contraction driven by myosin II filaments when bound to membrane tethered His_6-curly; scale bar: 1 µm.

(B) TIRF microscopy image (representing one field of view) of actin filaments (Alexa488) 20 min after addition of muscle myosin II filaments on His_6-curly containing SLBs; scale bar: 10 µm.

(C) TIRF microscopy image (representing one field of view) of actin filaments (Alexa488) 20 min after addition of muscle myosin II filaments on His_6-curly containing SLBs; scale bar: 5 µm.

(D) Dual color TIRF microscopy image of actin filaments (Alexa488, magenta) bound to membrane tethered fluorescently labelled His_6-SNAP-curly (Surface549, cyan) 20 min after addition of myosin II filaments; scale bar 5 µm.

(E) Model representing how myosin II filaments could drive the contraction of curly formed actin rings.

bioRxiv preprint doi: https://doi.org/10.1101/2020.07.10.197616; this version posted July 14, 2020. The copyright holder for this preprint (which was not certified by peer review) is the author/funder, who has granted bioRxiv a license to display the preprint in perpetuity. It is made available under aCC-BY 4.0 International license.

Figure 4

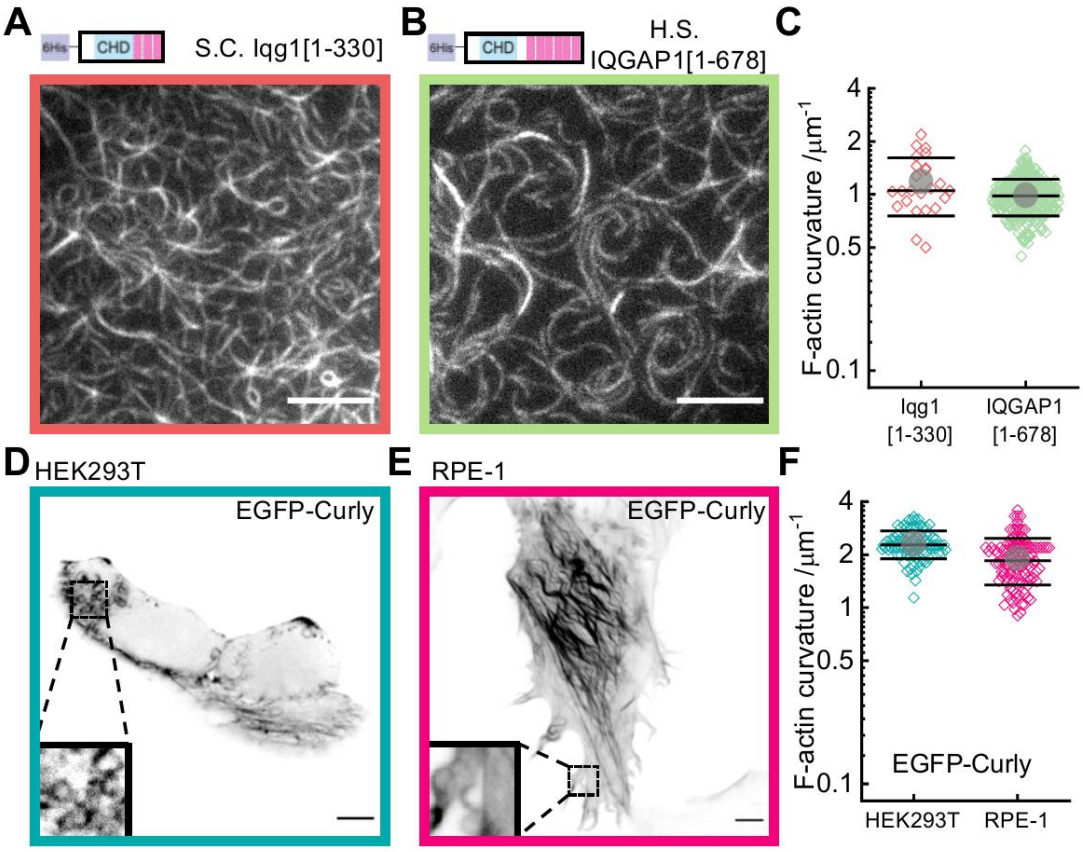

Figure 4 – Curly effect is conserved among species and it can foster actin bending in mammalian cells

(A) TIRF microscopy image of actin filaments (Alexa488) bound to membrane tethered His6-Iqg1[1-330] (*S. cerevisiae*); scale bar: 5 µm.

(B) TIRF microscopy image of actin filaments (Alexa488) bound to membrane tethered His6-IQGAP1[1-678] (*H. sapiens*); scale bar: 5 µm.

(C) Curvature measurements of actin filament rings and curved segments; shown are the individual data points and their mean ± s.d.; Iqg1[1-330] (orange): N = 167 from 12 field of views of 4 individual experiments; IQGAP1[1-678] (green): N = 407 from 20 field of views of 3 individual experiments.

(D) Confocal microscopy image (average intensity projection of the basal cell section) of a HEK293T cell transfected with EGFP-Curly, inlet shows zoom of dashed box; scale bar: 5 µm.

(E) Confocal microscopy image (average intensity projection of the basal cell section) of a REP-1 cell transfected with EGFP-Curly, inlet shows zoom of dashed box; scale bar: 5 µm.

(F) Curvature measurements of actin filament rings and curved segments found in EGFP-Curly expressing cells; shown are the individual data points and their mean ± s.d.; HEK293T (teal): N 91 from 14 cells of 2 individual experiments; REP-1 (fuchsia): N = 113 from 11 cells of 2 individual experiments.

bioRxiv preprint doi: https://doi.org/10.1101/2020.07.10.197616; this version posted July 14, 2020. The copyright holder for this preprint (which was not certified by peer review) is the author/funder, who has granted bioRxiv a license to display the preprint in perpetuity. It is made available under aCC-BY 4.0 International license.

Figure 4 – figure supplement 1

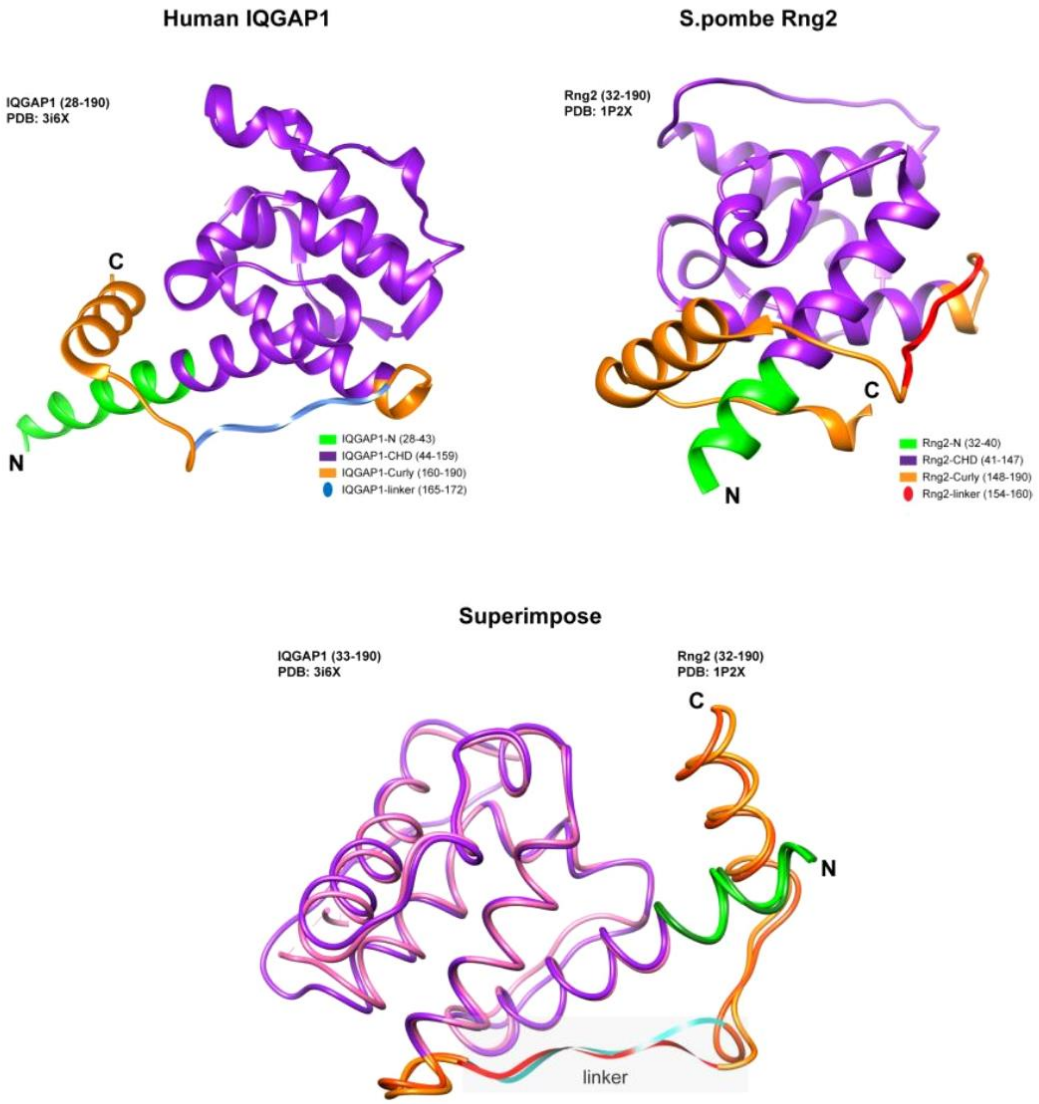

Figure 4-figure supplement 1
Depiction of structure predictions and overlay of *H. sapiens* IQGAP1[28-190] and *S. pombe* Rng2[32-190] indicating the strong similarity between the linker regions of both proteins that are thought to be important for actin bending.

bioRxiv preprint doi: https://doi.org/10.1101/2020.07.10.197616; this version posted July 14, 2020. The copyright holder for this preprint (which was not certified by peer review) is the author/funder, who has granted bioRxiv a license to display the preprint in perpetuity. It is made available under aCC-BY 4.0 International license.

Figure 4 – figure supplement 2

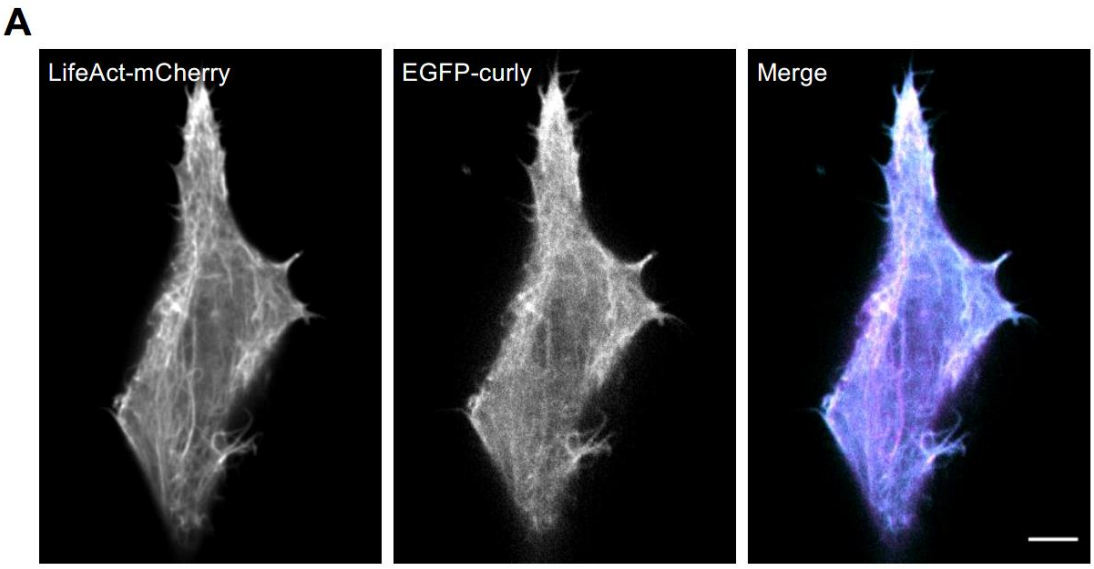

Figure 4-figure supplement 2
Dual color confocal microscopy image (average intensity projection of the basal cell section) of a HEK293T cell transfected with LifeAct-mCherry (magenta) and EGFP-Curly (cyan); scale bar: 5 µm.

bioRxiv preprint doi: https://doi.org/10.1101/2020.07.10.197616; this version posted July 14, 2020. The copyright holder for this preprint (which was not certified by peer review) is the author/funder, who has granted bioRxiv a license to display the preprint in perpetuity. It is made available under aCC-BY 4.0 International license.

Video captions

Video 1: TIRF microscopy image sequence of actin filaments (Alexa488) landing on His_6-curly decorated SLBs; scale bar: 5 µm.

Video 2: Example image sequence of an actin filament (Alexa488) bound to a His_6-curly decorated SLB displaying individual bending events after processing the image sequence with a Sobel filter to highlight the shape of the actin filament (the unprocessed images are shown in Figure 2-figure supplement 2); scale bar: 1 µm.

Video 3: Example image sequence of an actin filament (Alexa488, gray) with the plus end labelled by capping protein (SNAP647, yellow) landing on a His_6-curly decorated SLB; scale bar: 1 µm.

Video 4: Example image sequence of an actin filament (Alexa488, gray) with the plus end labelled by capping protein (SNAP647, cyan) landing on a curly-His_6 decorated SLB; scale bar: 1 µm.

Video 5: Example image sequences of actin filaments (Alexa488) polymerized by SLB tethered formin in the presence of His_6-curly bound to the SLB; scale bar 1 µm.

Video 6: Example image sequences of actin filaments (Alexa488) decorated with tropomyosin binding to membrane tethered His_6-curly; scale bar: 1 µm.

Video 7: Example image sequence showing formation, translation, and contraction of actin filament (Alexa488) rings on membrane tethered His_6-curly after the addition of muscle myosin II filaments; scale bar: 1 µm.

Video 8: Example image sequences of actin filament (Alexa488) ring contraction on membrane tethered His_6-curly after the addition of muscle myosin II filaments; scale bar: 1 µm.

bioRxiv preprint doi: https://doi.org/10.1101/2020.07.10.197616; this version posted July 14, 2020. The copyright holder for this preprint (which was not certified by peer review) is the author/funder, who has granted bioRxiv a license to display the preprint in perpetuity. It is made available under aCC-BY 4.0 International license.

Table 1: Plasmids used in this study

pET28C-6HIS-Rng2(1-189)	pSPW153
pET28C-6HIS-Rng2(1-250)	pSPW155
pET28C-6HIS-Rng2(1-300)	pSPW113
pET28C-6HIS-Rng2(1-147)	pSPW167
pET28C-6HIS-Rng2(41-147)	pSPW169
pET28C-6HIS-Rng2 (41-189)	pSPW187
pET28C-6HIS-Rng2 (41-250)	pSPW189
pET28C-6HIS-Rng2 (41-300)	pSPW191
pETMCN-Rng2(1-189)-C-6HIS	pSPW288
pETMCN-Rng2(1-250)-C-6HIS	pSPW290
pETMCN-Rng2(1-300)-C-6HIS	pSPW291
pET28C-6HIS-Rng2(1-189; Δ154-160)	pSPW297
pET28C-6HIS-Rng2(1-300; Δ154-160)	pSPW299
pET28C-6HIS-Curly100 (150-250)	pSPW284
pET23a-10HIS-SNAP-Rng2-CHD (1-300)	pSPW195
pET28C-6HIS-ScIqg1 (1-330)	pSPW200
pET28C-6HIS-HsIQGAP1 (1-678)	pSPW293
pCDNA3-EGFP-GSGG-Rng2(1-189)	pSPW620
pET-3d-6HIS-SNAP-tagged β1 subunit and untagged α1 subunits of chicken CapZ	Addgene: 69948 Bombardier et al., 2015
pET28C-6HIS-Cdc12 (740-1391)	pSPW123
pETMCN-AScdc8	pSPW036
pGEX4T1-GST-Fim1	pSPW114
pET23a-10HIS-SNAP-Ezrin-ABD	pSPW151
pGEX-alpha actinin4 (acnt4)	Gift from L. Blanchoin's lab